This is the peer-reviewed, final accepted version for American Mineralogist, published by the Mineralogical Society of America.
The published version is subject to change. Cite as Authors (Year) Title. American Mineralogist, in press.
DOI: https://doi.org/10.2138/am-2022-8888. http://www.minsocam.org/

Revision 1

Vapor-phases as Cu transport agents for the shear-zone-hosted mineralization system: A perspective from H–O–S–Cu isotopes

YUN ZHAO [1, 2, 3]*, CHUNJI XUE[1, 4]*, SHENG-AO LIU[1], RYAN MATHUR[5], XIAOBO ZHAO[1], REIMAR SELTMANN[6], JIANGANG JIAO[2], YONGSEN HUANG[7], XUEFENG WANG[8]

[1]*State Key Laboratory of Geological Processes and Mineral Resources, China University of Geosciences, Beijing 100083, China*

[2]*Key Laboratory of Western China's Mineral Resources and Geological Engineering. Ministry of Education, Chang'an University, Xi'an 710054, China*

[3] *Key Laboratory of Critical Minerals Metallogeny in University of Yunnan Province, Yunnan University, Kunming 650500, China*

[4]*The National 305 Project Office of Xinjiang, Urumqi 830000, China*

[5]*Department of Geology, Juniata College, Huntingdon, Pennsylvania 16652, USA*

[6]*Center for Russian and Central Eurasian Mineral Studies, Natural History Museum, Cromwell Road, London SW7 5BD, United Kingdom*

[7]*106 Geological Brigade of Sichuan Bureau of Geology and Mineral Resources, Chengdu 611130, China*

[8]*Yantai Geological Survey Center of Coastal Zone, China Geological Survey, Yantai 264004, China*

*Corresponding authors. E-mail: yun.zhao@cugb.edu.cn (Yun Zhao) or chunji.xue@cugb.edu.cn (Chunji Xue)

ABSTRACT

Elucidating metal transport agents is the key to understanding the genesis of deposits and tracking the locations of concealed orebodies. Here, we integrate H–O–S–Cu isotopic data from the shear-zone-hosted Lingyun Cu deposit, China as means to fingerprint metal transport agents. Sulfide mineralization can be divided into early and late stages, which consist of chalcopyrite + bornite + quartz veins and chalcopyrite + bornite + ankerite veinlets, respectively. Both $\delta^{18}O_{fluid}$ and δD values of fluid inclusions hosted by quartz ($\delta^{18}O_{fluid}$: 0.5‰ to 9.9‰, δD: −103.9‰ to −60.1‰) and $\delta^{65}Cu$ values of sulfides (−1.85‰ to +0.39‰) from the early stage progressively decrease from the southeastern to northwestern portions of the Lingyun deposit, whereas sulfide $\delta^{34}S$ simultaneously shifts toward heavier values (−14.4‰ to 5.0‰). The $\delta^{34}S$ and $\delta^{65}Cu$ values of sulfides from the late stage have restricted ranges from −11.2‰ to −9.3‰ and −0.30‰ to 0.05‰, respectively. The possibilities of meteoric water addition, water–rock interaction, inter-mineral Cu partitioning, diffusion and oxidation could be ruled out as reasons for having caused systematic H–O–S–Cu isotope variations. Vapor–liquid separation resulted in preferential incorporation of light Cu, H, and O isotopes into the vapor phase. The decrease in oxygen fugacity in the fluids resulted in a shift toward heavier $\delta^{34}S$ values as fluid flowed outward. Vapor-phases are the dominant transport agents for Cu in the Lingyun deposit, which may be widely applicable to shear-zone-hosted deposits. The direction of progressively increasing $\delta^{65}Cu$, δD, and $\delta^{18}O$ values and decreasing $\delta^{34}S$ values allows identification of potential locations of concealed orebodies.

Keywords: H–O–S–Cu isotopes; Cu transport agent; Shear-zone-hosted deposit; Tianshan

INTRODUCTION

Hydrothermal ore deposits serve as a primary resource of metals (Zajacz et al. 2017), which can be transported by both vapor and liquid phases (Williams-Jones and Heinrich 2005; Williams-Jones and Migdisov 2014). Elucidating metal transport agents is the key to understanding the genesis of deposits. The liquid and vapor phases exhibit rather different physical properties (e.g., temperature, pressure, and density), with the liquid phase concentrating in the hydrothermal center and vapor phase moving to the margin (Williams-Jones and Heinrich 2005; Heinrich 2007; Gruen et al. 2014). Utilizing such constraints provides a framework to track the locations of concealed orebodies reliably.

Direct approaches for the estimation of Cu transport agents in mineralization systems include fluid inclusion studies and experimental works. The microanalysis of fluid inclusions indicated that vapor phases contained higher Cu concentrations than coexisting liquid (e.g., Heinrich et al. 1992, 1999, Heinrich 2005; Williams-Jones and Heinrich 2005). However, this point of view has been challenged due to the possibility of Cu diffusion through quartz crystals (Lerchbaumer and Audétat 2012; Seo and Heinrich 2013). The pioneering experimental research has mainly focused on the Cu speciation and partition between vapors and liquids in porphyry mineralization systems at temperatures >450°C, with strong preferential partitioning of Cu in vapor phases (e.g., Pokrovski et al. 2008; Migdisov et al. 2014; Zajacz et al. 2017; Audétat 2019). It still needs to be clarified for the Cu transport agents in medium-low temperature (<400°C) Cu mineralization systems.

The medium-low temperature (<400°C) shear-zone-hosted Cu deposits are a recently discovered type of mineralization (e.g., Zheng et al. 2012; Kitt et al. 2016; Höhn et al. 2017;

Zhao et al. 2018), which provides an appropriate target to clarify Cu transport agents for this system. However, experimental studies are unavoidably hampered due to the knowledge gap for this still poorly constrained mineralization system. The application of H–O–S stable isotopes has significantly enhanced our understanding of the hydrothermal mineralization systems (e.g., Ohmoto 1986; Rye 1993; Sheppard and Gustafson 1976; Taylor 1997; Hoefs 2009, 2018). Copper isotopes have been used to track diverse geological processes, such as fluid extraction from the source (Zhou et al. 2013; Guo et al. 2020), vapor–liquid separation (Seo et al. 2007; Rempel et al. 2012; Gregory and Mathur 2017), fluid flow pathways (e.g., Li et al. 2010; Mathur et al. 2013; Wu et al. 2017), and mineral precipitation (Li et al. 2010; Maher and Larson 2007). Thus, integrating H–O–S–Cu isotopic data can provide alternative and reliable insights into metal transport agent. The shear-zone-hosted Lingyun Cu deposit is located in the Tianshan orogenic belt, providing an appropriate target to clarify Cu transport agent for this type of deposit. Our findings suggest that integrating H–O–S–Cu isotopic analyses in concert with geochemical modeling reveals vapor-phase as the dominant metal transport agent in a metamorphic geological environment.

GEOLOGICAL SETTING

The Central Asian Orogenic Belt (CAOB) extends from the Pacific Ocean to the European Craton (Fig. 1A, Sengör et al. 1993; Windley et al. 2007; Xiao et al. 2009; Jiang et al. 2014), which is composed of a series of ancient microcontinents, volcanic rocks, and passive margin sequences (Pirajno 2010; Pirajno et al. 2011). Tianshan is situated along the southern margin of the CAOB. The Chinese portion can be further subdivided into the

Yili–Kazakhstan Block (YKB), the North Tianshan Orogenic Belt (NTOB), the Central Tianshan Terrane (CTT), and the South Tianshan Orogenic Belt (STOB) (Fig. 1B; Gao et al. 2009; Jiang et al. 2014; Qian et al. 2009; Wang et al. 2016a, b, c, 2018). Rotation of the Siberian and Tarim blocks resulted in extensive strike-slip shear activities along the boundaries of the YKB, NTOB, CTT, and STOB, with the development of steeply dipping mylonitic foliations (Fig. 1A, B; Wang et al. 2007; Pirajno 2010, 2011). Systematic Ar–Ar and U–Pb ages indicate that extensive shearing of the main suture zone in Tianshan occurred during late Carboniferous to Permian (310–260 Ma, Xu et al. 2011; Cai et al. 2012; Konopelko et al. 2007, 2009). The extensive shearing was accompanied by the development of Au mineralization along the boundaries of YKB, NTOB, CTT, and STOB (e.g., Sawayaerdun, Wangfeng, Kangguer, Matoutan and Shiyingtan, Chen et al. 2012a,b; Zhang et al. 2003, 2004; Han et al. 2006; Mao et al., 2005).

Ductile to brittle shear zones along the northern margin of the STOB control the formation of shear-zone-hosted Au–Cu mineralization systems (e.g., Baijianshan, Wolonggang and Yanxingshan, Yakubchuk et al. 2002; Zhao et al. 2018; Xue et al. 2020). The Lingyun deposit contains 4.73 million tonnes of ore with 1.3 wt% Cu (Chen 2008; Zhao et al. 2018), which has been mined since 2009. The Permian Lingyun deposit is hosted by the Devonian Aerbishibulake Formation with greenschist-facies metamorphism (Fig. 1C, e.g., Chen 2008). The silicate minerals and coexisted sulfide assemblages develop linear fabrics (Fig. 2A–D), both of which parallel to the regional shear zones. Silicification, sericitization, and carbonatization are well developed around the orebodies and shear zones, and these alteration types are spatially associated with Cu mineralization (Fig. 2A–C). The Cu

mineralization (Chalcopyrite Re–Os dating, 297.9 ± 3.4 Ma) developed coevally with metamorphic and deformation events in the area (Sericite Ar–Ar dating, 292.3 ± 2.4 Ma) (Zhao et al. 2018). No igneous intrusions have been discovered other than a few diorite dikes crosscutting the wall rocks and orebodies (Fig. 1C).

Resource evaluation drillings have been widely utilized to constraint the grade, tonnes and mining/metallurgical characteristics of the potential orebodies (Marjoribanks, 2010). A prospect line consists of several drill holes, parallel to the trend of the orebodies (e.g., prospecting line 136, Fig. 1D). In the Lingyun deposit, the prospect lines are numbered from southeast to northwest (prospecting line 140 to 90, Fig. 1C). Twelve variably sized orebodies have been discovered in the Lingyun mine area, among which ~85% Cu resource occur from prospecting line 138 to line 124. The distribution and orientation of orebodies are closely controlled by the regional shear zone, striking toward west and dipping toward south (Fig. 1D). Detailed geological survey elucidates that the volume of alteration minerals and spatial extent of alteration zones decreases laterally and vertically away from prospecting line 138 to line 90 (Fig. 1C). The paragenetic stages of primary sulfides recognized based on crosscutting relationships are: (1) early-stage fault-controlled chalcopyrite- and bornite-bearing quartz veins and lenses aligned parallel to the foliation within the crystal tuff, which comprises albite + sericite ± epidote assemblages (Fig. 2A, C–F); and (2) late-stage assemblages of ankerite + chalcopyrite + bornite within veinlets (Fig. 2B). The early-stage mineralization provides 80–90% Cu resource in the Lingyun deposit. Primary sulfide minerals are mainly chalcopyrite and bornite with minor pyrite and pyrrhotite (Fig. 2A–E). Chalcopyrite and bornite commonly coexist (Fig. 2D, F). Pyrite occurs as inclusions within

chalcopyrite and gangue minerals (Fig. 2E). Secondary Cu-bearing minerals precipitated in supergene environments include chalcocite, digenite, and covellite (Fig. 2D, F). The fresh samples were collected from open pits of the 1100 m, 1150 m, 1170 m and 1190 m levels (at depths of 10 m, 30 m, 50 m and 100 m below surface, respectively) from prospecting line 138 to line 90 (Table 1 and 2, Fig. 3). The coexisting sulfide mineral pairs in the same sample are in textural contact of equilibrium (Table 2, Fig. 2F).

SAMPLES AND ANALYTICAL METHODS

Analysis of hydrogen and oxygen isotopes

Hydrogen isotope ratios of fluid inclusions hosted by quartz (n = 37) and oxygen isotope ratios of quartz grains (n = 37) of the early-stage veins were analyzed by a Finnigan MAT-253 mass spectrometer at the Beijing Research Institute of Uranium Geology, China. Oxygen was liberated by reaction with BrF_5 (Clayton and Mayeda 1963), and converted to CO_2 on a platinum-coated carbon rod for O isotope analysis. The water of the fluid inclusions in early-stage quartz veins was released by heating the quartz grains to >500 °C and then reacted with chromium powder at 800 °C to obtain H for isotope analysis (Coleman et al. 1982). The isotope data were reported in standard δ-notation in per mil (‰) deviation relative to Standard Mean Ocean Water (SMOW). The analytical precisions are ± 2‰ for δD and ± 0.2‰ for $\delta^{18}O$.

Analysis of sulfur isotopes

Sulfur isotope compositions were measured at the Beijing Research Institute of Uranium

Geology. Approximately 15 mg of sulfide minerals (<80 mesh) from the early and late stage veins (n = 50) or 30 mg of whole-rock powders (<200 mesh) from wall rocks (n = 6) without mineralization and hydrothermal alteration were mixed with 150 mg Cu_2O and heated at 1050 °C under vacuum to extract SO_2. The collected SO_2 were analyzed for S isotope compositions using a Finnigan MAT-253 mass spectrometer. The results were expressed as $\delta^{34}S$ per mil (‰) relative to the Vienna Canyon Diablo Troilite (V-CDT), with analytical precision better than ± 0.2‰.

Analysis of copper isotopes

Sulfide ores selected from the early and late stage veins were crushed to <80 mesh, from which chalcopyrite and bornite were separated by conventional heavy liquids, then carefully handpicked under a binocular microscope to reach a purity of better than 95%. The detailed procedures for sample digestion, chemical purification, and isotope measurement followed those presented by Liu et al. (2014a, b, 2015) modified from Maréchal et al. (1999).

Sulfide mineral separates (<0.1 mg, n = 50) and wall-rock powders without mineralization and hydrothermal alteration (25 mg, n = 6) were digested in mixed solutions of purified HNO_3 and HCl at 130 °C. After dissolution, 1 ml of 8 N HCl + 0.001% H_2O_2 was added to the beaker and heated to dryness. This process was repeated three times to convert all cations into chloride species. Copper was purified by ion-exchange chromatography using the anion resin AG-MP-1 M. The Cu recovery and procedural blank were >99.7% and <2 ng, respectively.

Copper isotope measurements were performed using a Neptune plus MC–ICP–MS

instrument at the Isotope Geochemistry Laboratory of the China University of Geosciences, Beijing, China. A sample–standard bracketing method was utilized for instrumental mass fractionation and drifting correction (Zhu et al. 2002; Liu et al. 2014a). A measurement is composed of 4 blocks of 40 cycles, yielding each value with an average of 160 ratios. Copper isotopic data are reported against SRM NIST976 in δ-notation in per mil (‰), where $\delta^{65}Cu = ((^{65}Cu/^{63}Cu)_{sample}/(^{65}Cu/^{63}Cu)_{standard} - 1) \times 1000$. The external reproducibility for $\delta^{65}Cu$ measurements based on repeated analyses of reference standards (BHVO-2, United States Geological Survey) was better than ±0.05‰ (2SD). The solutions for Cu isotope analysis were also measured for Cu/Fe ratios using an ICP–OES to test the purity of sulfides, and the analytical precision was better than 5%.

RESULTS

Hydrogen and oxygen isotope ratios

The $\delta^{18}O_{quartz}$ values range from 5.8‰ to 15.6‰ with a mean of 12.0 ± 0.80‰ (n = 37). The $\delta^{18}O_{fluid}$ values were estimated by the equilibrium equation from Clayton et al. (1972) (Equation 1).

$$1000\ln\alpha_{quartz-fluid} = 3.38 \times 10^6 \times T^{-2} - 3.40 \quad (1);$$

where homogenization temperatures (T) were obtained by microthermometry of fluid inclusions (Table 1; Fig. 4). The mean homogenization temperatures of each sample were used to calculate the $\delta^{18}O_{fluid}$ values of fluid inclusions, with a range of 0.5‰ to 9.9‰ (Table 1; Figs 3 and 4). The δD values range from −103.9‰ to −60.1‰ (Table 1; Figs 3 and 4). Both $\delta^{18}O_{fluid}$ and δD values progressively decrease from prospecting line 138 to line 90

(Table 1; Figs 3 and 4).

Sulfur isotope ratios

The $\delta^{34}S$ values of sulfide minerals from the early stage in the Lingyun deposit range from −14.4‰ to 5.0‰ with a mean of −5.6‰ (n = 44, Fig. 3). The $\delta^{34}S$ values of sulfides from the late stage have a restricted range from −11.2‰ to −9.3‰ (n = 6, Fig. 3). The wall rocks have much heavier S isotopic compositions than those of the sulfides, ranging from 3.3‰ to 6.6‰ ((n = 6, Fig. 3). The $\delta^{34}S$ values of chalcopyrite are similar to those in coexisting bornite (within ±0.6‰, Fig. 3), a much smaller variation than the S isotopic variations at the scale of the orebody (8.3‰, Fig. 3). The $\delta^{34}S$ shifts toward heavier values from prospecting line 138 to line 90 (Table 2; Fig. 3).

Copper isotope ratios

The Cu/Fe ratios of chalcopyrite and bornite from the early stage in the Lingyun deposit show a restricted range from 0.96 to 1.16 and 4.93 to 5.05, consistent with the stoichiometric ratios of the minerals (Cu/Fe = 1 for chalcopyrite and Cu/Fe = 5 for bornite). The $\delta^{65}Cu$ values of the sulfide minerals have a wide range from −1.85‰ to +0.39‰ (n=50, Fig. 3), with a mean of −0.79‰ ± 0.44‰ (1σ). In contrast, the $\delta^{65}Cu$ values of the wall rocks show a narrow range from −0.67‰ to −0.63‰ (n=6, Fig. 3). Coexisting chalcopyrite and bornite exhibit similar Cu isotopic compositions (within ±0.3‰, Fig. 6). The $\delta^{65}Cu$ values shift toward lighter values from prospecting line 138 to line 90 (Table 2; Fig. 3).

DISCUSSION

Mechanisms for developing systematic variations in H–O–S–Cu isotopic compositions

The volume of alteration minerals, spatial extent of alteration zones, and homogenization temperatures of fluid inclusions decrease and vapor/liquid ratios of fluid inclusions increase from prospecting line 138 to line 90 (Fig. 1C, Table 1, Zhao et al. 2018), both of which are indicative of the pathway of hydrothermal fluids flowing outward from the hydrothermal center to peripheral regions. The changes of physicochemical conditions as fluids flowing trigger mineralization as well as develop systematic variations in H–O–S–Cu isotopic compositions.

Hydrogen and oxygen isotopes. In general, the H–O isotopic compositions of fluids are commonly influenced by the isotopic composition of the initial fluid and wall rocks, as well as temperature and the water/rock ratio (W/R) (Ohmoto 1986; Taylor 1997; Hoefs 2009, 2018). Simple mass-balance calculations (Equation 2–4; Taylor 1974) indicate that addition of meteoric water or water–rock interaction may have occurred in the Lingyun deposit (Fig. 4A, B).

$$W \times \delta i_{water} + R \times \delta^{i}_{rock} = W \times \delta^{f}_{water} + R \times \delta^{f}_{rock} \quad (2)$$

$$W/R = (\delta^{f}_{rock} - \delta^{i}_{rock}) / [\, \delta^{i}_{water} - (\delta^{f}_{rock} - \Delta)] \quad (3)$$

$$\Delta_{rock\text{-}water} = \delta^{i}_{rock} - \delta^{f}_{water} \quad (4)$$

where i = initial value, f = final value after exchange, W = atomic percent of fluid, and R = atomic percent of exchangeable rock; The mass ratio of water to rock was calculated using w(W)/w(R) =0.5 × W/R for the calculation of $\delta^{18}O$ and w(W)/w(R) = 0.01 × W/R for δD.

However, the significant input of meteoric water cannot cause the progressively

decreasing of the $\delta^{18}O_{fluid}$ and δD values from the prospecting line 138 to line 90 (Fig. 3). Water–rock interaction would have resulted in Cu and S isotopic compositions in the sulfides similar to those of the wall rocks. However, the Cu isotopic compositions of the sulfides show a much wider range than that of the wall rocks (Fig. 3), and their $\delta^{34}S$ values are much lower than those of the wall rocks, indicating negligible influence on isotopic compositions by water–rock interaction.

Vapor (e.g., H_2O, CH_4, and CO_2)–liquid separation is another means of fractionating H–O isotopes, in which the vapor is relatively enriched in lighter O isotopes (Horita and Wesolowski 1994; Zheng 1993). Experimental results have shown that water vapor preferentially incorporates more deuterium than liquid water at 230–350 °C (Horita and Wesolowski 1994). Homogenization temperatures for early-stage fluid inclusions are >230 °C (Zhao et al. 2018), and should have caused enrichment in deuterium in the water vapor. However, CH_4, a common vapor phase in the Lingyun deposit (e.g., Zhao et al. 2018), would incorporate deuterium (Fig. 6C; Richet et al. 1977; Hoefs 2009, 2018). The Rayleigh distillation equations (Equation 5–6; Sharp 2017) were used to simulate H–O isotope fractionation caused by vapor–liquid separations. The isotope fractionation factors for H_2O and CH_4 were estimated by the equations of Horita and Wesolowski (1994) (Equation 7–8) and Richet et al. (1977) ($\alpha_{vapor–liquid}$ = 0.8772), respectively.

$$\delta X_{vapor}\ (‰) = (\delta X^{i}_{vapor} + 1000) \times F^{(\alpha-1)} - 1000 \quad (5)$$

$$\delta X_{liquid}\ (‰) = 1/\alpha \times (\delta X_{vapor} + 1000) - 1000 \quad (6)$$

$$10^3 \ln \alpha_{vapor\text{-}liquid}\ (D) = 1158.8 \times (T^3/10^9) - 1620.1 \times (T^2/10^6) + 794.84 \times (T/10^3) - 161.04 + 2.9992 \times (10^9/T^3) \quad (7)$$

$$10^3 \ln \alpha_{\text{vapor-liquid}} (^{18}O) = -7.685 + 6.7123 \times (10^3/T) - 1.6664 \times (10^6/T^2) + 0.35041 \times (10^9/T^3) \quad (8)$$

where δX_{vapor} is the isotopic composition of the vapor for a given value of F, δX_{liquid} is the isotopic composition of the liquid, $\delta X^{\text{i}}_{\text{vapor}}$ is the isotopic composition of the initial vapor, α is the fractionation factor between the product of reaction and the substrate of reaction, F is the fraction of vapor remaining, and T is Kelvin temperature.

Furthermore, the H–O isotopic compositions of cumulative and instantaneous liquids and vapor during vapor liquidation were calculated based on Rayleigh equations (Equation 9–11; Guo et al. 2020).

$$\delta X_{\text{evolved phase}} = (\delta X_{\text{initial phase}} + 1000) \times f^{\alpha - 1} - 1000 \quad (9)$$

$$\delta X_{\text{instantaneous product}} = (\delta X_{\text{initial phase}} + 1000) \times \alpha \times f^{\alpha - 1} - 1000 \quad (10)$$

$$\delta X_{\text{cumulative product}} = (\delta X_{\text{initial phase}} + 1000) \times (f^{\alpha} - 1) / (f - 1) - 1000 \quad (11)$$

Where $\delta X_{\text{initial phase}}$ refers to the isotope ratios of the initial vapor; $\delta X_{\text{evolved phase}}$ refers to the isotope ratios of the evolved vapor; $\delta X_{\text{instantaneous product}}$ is the isotope ratios of instantaneous liquid; $\delta X_{\text{cumulative product}}$ represents the isotope ratios of cumulative liquid that reaches isotope equilibrium again; α is the isotope fractionation factor between vapor and liquid; f is the fraction of H and O remaining in vapor.

Our calculations indicate that vapor–liquid separation likely contributed to the observed H–O isotopic variation of the Lingyun deposit (Fig. 4C and 4D). By contrast, vapor liquidation cannot solely produce the H–O isotopic variation (Fig. 4E and 4F). If so, the vapor phase that incorporated light H and O isotopes migrated away to a greater distance than liquid, consistent with decreasing $\delta^{18}O_{\text{fluid}}$ and δD values from prospecting line 138 to line 90

(Fig. 3).

S isotopes. The S isotopic compositions of sulfides that precipitated from hydrothermal fluids are controlled by numerous factors, including: (1) the isotopic composition of the hydrothermal fluids, (2) physicochemical conditions (e.g., temperature, pH, and fO_2), and (3) the mineral assemblages that precipitates from the fluid (e.g., Hoefs 2009, 2018). Coexisting chalcopyrite and bornite have similar S isotopic compositions (Fig. 3), precluding the possibility of significant isotope exchange between these minerals. Numerical modeling indicates that the $\delta^{34}S$ of sulfides precipitated from a common hydrothermal fluid shift toward lighter values with cooling, irrespective of fO_2 (e.g., Rye 1993; Wilson et al. 2007), which contrasts with our observations from the Lingyun deposit (Fig. 3).

Reactions between CO_2-bearing hydrothermal fluids and wall rock that lead to the formation of Ca–Mg–Fe carbonates (e.g., ankerite) can cause oxidation of the fluid (McCuaig and Kerrich 1998). Hydrothermal oxidation can also occur during vapor–liquid separation owing to preferential partitioning of reduced volatile species (e.g., H_2) into an immiscible H_2O–CO_2 ± CH_4-rich phase (Drummond and Ohmoto 1985; Golding et al. 1990; Palin and Xu 2000). The physicochemical conditions (e.g., alteration, mineral assemblages, logfO_2, and pH) were estimated (Fig. 3) from phase stability relationships using the software SUPCRT92 (Johnson et al. 1992) with the database provided by Zimmer et al. (2016). The early-stage chalcopyrite + bornite + sericite + albite assemblages indicate constant intermediate pH conditions, with a decrease in fO_2 as the fluids cooled (Fig. 3). At intermediate temperatures, pressures, and pH, the main reduced and oxidized S species in hydrothermal fluids (Fig. 2) relate to the equilibrium reaction of $H_2S + 4H_2O = HSO_4^- + H^+ + 4H_2$ (Palin and Xu 2000).

Oxidized S species tend to incorporate heavy S isotopes relative to reduced species under equilibrium, with ^{34}S and ^{32}S enrichment in HSO_4^- and H_2S, respectively (Fig. 5). Preferential enrichment of the sulfides in lighter S isotopes relative to the wall rocks (Fig. 3) can be explained by hydrothermal oxidation. As the hydrothermal fluids flowed laterally and vertically, precipitation of Cu-bearing sulfides would facilitate the reaction $HSO_4^- + H^+ + 4H_2 = H_2S + 4H_2O$ and a decrease in fO_2 (Fig. 5). Rayleigh equations (Equation 9–11; Guo et al. 2020) were used to simulate the S isotope ratios during sulfide precipitation (Fig. 6). Modeling results indicate that fO_2 variation as the fluids cooled needed to be invoked to explain the $\delta^{34}S$ range in the Lingyun sulfides (Figs. 3 and 6). The Cu-bearing sulfides that were precipitated from evolved hydrothermal fluids preferentially incorporated heavier S isotopes compared with the original fluids (Fig. 3).

Copper isotopes. Possible mechanisms that may lead to significant Cu isotope fractionation in hydrothermal systems include inter-mineral Cu partition, diffusion, oxidation, fluid mixing, water-rock interaction, Cu mobilization from source to fluid, Cu transport, and deposition of Cu-bearing minerals (e.g., Li et al. 2010; Mathur et al. 2010; Maher et al. 2011; Rempel et al. 2012). The Cu isotopic compositions are similar between coexisting bornite and chalcopyrite (<0.3‰ for $\delta^{65}Cu$, Fig. 6), much smaller than the isotopic variations on the orebody scale (~1.5‰ for $\delta^{65}Cu$, Fig. 6).

Diffusion can result in significant Cu isotope fractionation (Williams and Archer 2011), which is driven by chemical and thermal gradients (e.g., Zhao et al. 2017). However, at least two lines of evidence exclude the diffusion-driven $\delta^{65}Cu$ variation in the Lingyun deposit (Fig. 3). First, Cu transport in liquids and vapors is much faster than the diffusion rate of Cu (e.g.,

Li et al., 2010). Second, diffusion-driven processes would enrich the locations with high Cu concentrations and temperatures in heavy Cu isotopes (Williams and Archer 2011). However, the orebodies with highest Cu contents (Lines 128–130) have Cu isotopic compositions that are similar to those of the sulfide mineral-poor wall rocks (Fig. 3).

Recent experiments (Guo et al. 2020) indicate that fluid phases preferentially incorporate heavy Cu isotopes relative to coexisting silicates at 800 to 850 °C, depending on Cu speciation. Redox-related Cu isotope fractionation seems more plausible in the Lingyun deposit, as the temperature for the metamorphic event (greenschist facies, <500 °C, Zhao et al. 2018) is much lower than the temperature range of the water-saturated solidus in igneous rocks (Guo et al. 2020). Thus, metamorphic devolatilization enriched the exsolved fluids (Lines 134–138, Fig. 3) in heavier Cu isotopes relative to the wall rocks due to redox reactions (−0.65‰ to −0.05‰, Fig. 3). Similarly, synorogenic mineralization hosted by greenschist that was driven by metamorphic fluids has δ^{65}Cu ranges of −0.26‰ to 0.36‰ and −0.44‰ to 0.08‰ in the Kupferberg deposit (Höhn et al. 2017) and the Archaean Hattu schist belt (Molnár et al. 2016), respectively. Significant water–rock interaction will shift the δ^{65}Cu of fluids toward similar values with wall rocks. However, the δ^{65}Cu values of the sulfide minerals (−1.85‰ to +0.39‰) have a much wider range than the wall rocks (−0.67‰ to −0.63‰, Fig. 3). Although the mixing of meteoric water would change the Cu isotopes toward isotopically heavy values, this process may occur when vapor-like fluids dominated the Cu isotope shifts toward low values. The locations with inclusions exhibiting high vapor/liquid ratios (prospecting line 90) have low δ^{65}Cu values (Fig. 3), which precludes the possibility of mixing of meteoric water causing significant δ^{65}Cu variation.

In the liquid phase, Cu is present mostly as CuHS over a wide pH range (from ~4.5 to ~11) at temperatures of 200 °C to 350 °C (Williams-Jones and Migdisov 2014). In the vapor phase, Cu occurs predominantly as CuHS or Cu(HS)(H_2S) (Pokrovski et al. 2008; Seo et al. 2009; Etschmann et al. 2010; Rempel et al. 2012), with minor chloride species (Rempel et al., 2012). Experimental and theoretical considerations indicate that the stoichiometries of chalcopyrite and bornite are dominated by $Cu^{+}Fe^{3+}S_2^{2-}$ (Klekovkina et al. 2014) and $Cu_5^{+}Fe^{3+}S_4^{2-}$ (Van der Laan et al. 2002; Ding et al. 2005), respectively. In summary, Cu occurs as +1 valence in hydrothermal liquids, vapor, and primary sulfides (bornite and chalcopyrite, Goh et al. 2006; Pearce et al. 2006), ruling out the possibility of redox-driven Cu isotope fractionation during Cu transport and precipitation for the Lingyun deposit.

Theoretical calculations indicate that the aqueous fluids consist of up to 80%–90% vapor in boiling hydrothermal systems (Cline and Bodnar 1991; Landtwing et al. 2010). Copper is highly volatile in hydrothermal systems (Li and Audétat 2012, 2015), and thus can be transported in significant quantities in vapor phases ($D_{Cu}^{vapor/fluid}$ = 0.2–0.7, Simon et al. 2006; Pokrovski et al. 2008; Rempel et al. 2012). Quantum chemical calculations indicate that ^{65}Cu tends to concentrate in vapor phases as Cu_3Cl_3 (Seo et al. 2007). In contrast, experimental studies suggested that ^{63}Cu is preferentially enriched in vapor phases as CuHS (Maher et al. 2011; Rempel et al. 2012; Guo et al. 2020), which is the common compound in nature (Heinrich et al. 1999; Pokrovski et al. 2008). Furthermore, extensive experimental studies on other metal isotopes, such as Hg (Estrade et al. 2009; Zambardi et al. 2009), Fe (Wang et al. 2001), Mg (Wang et al. 2001; Richter et al. 2007), and Ca (Wombacher et al. 2008), have suggested that vapor phases tend to incorporate lighter isotopes than liquids. Thus, we

suggest that the vapor phase was more likely enriched in ^{63}Cu relative to ^{65}Cu as CuHS. The Rayleigh distillation equations (Equation 5–6; Sharp 2017) were utilized for simulating Cu isotope variation during vapor–liquid separations, which can produce the Lingyun $\delta^{65}Cu$ ranges (Fig. 7A).

Thermodynamic estimations (Fig. 5) indicate that Cu was dissolved dominantly as CuHS, with or without minor $CuCl_2^-$, in the Lingyun deposit (Williams-Jones and Migdisov 2014). Quantum chemical calculations indicate that Cl^- and HS^- exhibit a similar degree of fractionation of Cu isotopes (Seo et al. 2007). Thus, Cu transport by liquids as CuHS and $CuCl_2^-$ will not cause systematic Cu isotopic variations. The Cu isotope fractionation factor during chalcopyrite precipitation has been experimentally determined minimal ($\alpha_{liquid-chalcopyrite}$ from 0.9998 to 1, Maher et al. 2011). The evolution of $\delta^{65}Cu$ values of different phases in the shear-zone-hosted mineralization system has been modeled by Rayleigh fractionation equations (Equation 9–11; Guo et al. 2020). Numerical calculations indicate that the final precipitation of Cu-bearing minerals in the peripheral regions results in a limited isotopic shift (Fig. 8B), as Cu is strongly chalcophile and expected to inherit the isotopic compositions of the ore-forming liquids.

The models for H–O–S–Cu isotope fractionation in the shear-zone-hosted Lingyun Cu deposit

Ductile to brittle shear zones have long been recognized as sites for epithermal mineral deposition (Sibson et al. 1975; Sibson 1986, 1987, 2004). The formation of shear-zone-hosted deposits commonly involves three stages (Chen et al. 2004, 2006; Heinrich 2007; Phillips and

Powell 2009, 2010; Précigout et al. 2017): (1) metamorphic devolatilization and metal mobilization, (2) transport of metal by vapor and liquid, and (3) precipitation of the metal as sulfides. During stage 1, wall rocks underwent syncollisional deformation and metamorphism, during which large amounts of CO_2-rich fluids generated (Zhao et al. 2018) and migrated upward in the Lingyun area (Fig. 9). Reaction of these CO_2-rich fluids with the wall rocks resulted in the formation of Fe-carbonates (e.g., ankerite) and caused oxidation of the fluids (Palin and Xu 2000). The metamorphic affinity of the fluids, as indicated from the H–O isotopic data (Figs 3, 4, and 9), remobilized and extracted Cu and S from the wall rocks during upward migration. The exsolved fluids preferentially incorporated lighter S and heavier Cu isotopes relative to the wall rocks owing to oxidation of the fluids (Figs 3 and 9). In contrast, the change in oxidation state did not cause significant H–O isotope fractionation, as H and O isotopes have exclusive ionic valences (H^+ and O^{2-}, respectively).

When the Cu-bearing fluids reached the brittle–ductile transition, a substantial amount of Cu was precipitated as a result of fracturing and associated drops in pressure (Figs 3 and 9; Zhao et al., 2018). These sulfides inherited the Cu and S isotopic compositions of the instantaneous equilibrium fluids in prospecting line 138 (Figs 3 and 9). A significant decrease in pressure would also have resulted in vapor–liquid separation (Zhao et al. 2018), with vapor phases incorporating lighter Cu isotopes than liquids (Figs 3 and 9; Pokrovski et al. 2008; Rempel et al. 2012). Within the temperature range of the Lingyun deposit, enrichment in reduced volatile species (e.g., H_2O, CH_4, and CO_2) within the vapor phase would have resulted in preferential incorporation of isotopically lighter H–O relative to liquids (Figs 3 and 9).

The Cu-bearing vapor and liquids moved outward both laterally and vertically from prospecting line 138 toward line 90 (Fig. 9), of which vapor was more abundant. Copper was transported in significant quantities in the vapor relative to coexisting liquids (Simon et al. 2006; Pokrovski et al. 2008), and the vapor preferentially incorporated light Cu isotopes (Fig. 9). Thereafter, cooling would have promoted progressive condensation of the Cu-bearing vapors, shifting the δ^{65}Cu of the sulfides toward lighter values from prospecting line 138 to 90 (Figs 3 and 9).

Similarly, preferential enrichment in light H and O isotopes within the vapor phase and its subsequent condensation on migration would have brought about decreasing $\delta^{18}O_{fluid}$ and δD values in the condensed liquids (Figs 3 and 9). The progressive precipitation of Cu-bearing sulfides as the liquids moved outward (Figs 3 and 9) would have caused HSO_4^-/H_2S ratios in solution to increase. The reduced volatile species (e.g., H_2, CO_2, and CH_4) dissolved in the evolved liquids in the peripheral regions (e.g., prospecting line 90) of the deposit would have contributed to more reducing conditions (Fig. 5). Both the precipitation of sulfides and dissolution of volatile species would have resulted in progression of the reaction $H^+ + 4H_2 + HSO_4^- = H_2S + 4H_2O$. In this way, sulfides that formed at the margins of the deposit preferentially incorporated heavy S isotopes (Figs 3 and 9). The δ^{34}S and δ^{65}Cu values of sulfides from the late stage have restricted ranges without systematic spatial variations, which potentially indicate a liquid-phase-dominated transport for Cu in this stage (Figs 3 and 9).

IMPLICATIONS

Elucidating metal transport agents is the key to understanding the genesis of deposits and further tracking the concealed orebodies (Williams-Jones and Heinrich 2005; Heinrich 2007; Gruen et al. 2014; Zajacz et al. 2017). It is conventionally suggested that the onset of boiling triggers significant metal precipitation (Zajacz et al. 2017; Zhao et al. 2018). On the other hand, fluid boiling in hydrothermal systems would significantly separate vapor and liquid phases, among which vapor phases serve as important transport agents for Cu in shear-zone-hosted deposits. Subsequently, Cu-bearing vapors move outward from the hydrothermal center to peripheral regions.

Shear-zone-hosted deposits have generally undergone multiple stages of metamorphism, accompanied by extensive shearing along the main suture zone (e.g., Chen et al. 2004, 2006; Goldfarb et al. 2004, 2005; Pirajno 2009, 2010; Phillips and Powell 2009, 2010). Ductile to brittle shear zones provide channels for metal-bearing vapor and liquids flowing outward. Successive fluid boiling is triggered as metal-bearing liquid flow promotes the gradual sulfide deposition and further generations of vapors. From this perspective, metal precipitations can occur along the shear zone over a long distance, because vapor phases can move outwards promptly. Thermodynamic modeling indicates that Cu can be extracted from metamorphic rocks by autogenous fluids upon crossing the greenschist–amphibolite facies boundary (Zhong et al., 2015). Vapor phases may widely serve as important transport agents for Cu in greenschist–amphibolite facies metamorphism systems. The integrating H–O–S–Cu isotopic data can be regarded as a reliable tracer for tracking metal transport agents and provide new insights for mineral exploration.

ACKNOWLEDGEMENTS

We are grateful to Dandan Li, Ze-Zhou Wang and Yiwen Lv for their assistance in the lab. We thank Stefan Höhn for his comments on the early version of this manuscript. We extend our gratitude to two anonymous reviewers for their constructive comments and the Editor Prof. William H. Peck for his editorial input. This research is jointly supported by the National Key Research Program of China (2022YFF0800902), the Fundamental Research Funds for the Central Universities, CHD (300102263505), the Research Startup Project of Yunnan University (YJRC4201804), the National Natural Science Foundation of China (41803013), and the Fundamental Research Funds for the Central Universities (QZ05201905).

REFERENCES CITED

Audétat, A. (2019). The metal content of magmatic-hydrothermal fluids and its relationship to mineralization potential. Economic Geology, v. 114, p. 1033–1056.

Baker, T., Van Achterberg, E., Ryan, C.G, and Lang, J.R. (2004) Composition and evolution of ore fluids in a magmatic-hydrothermal skarn deposit. Geology, v. 32, p. 117–120.

Cai, Z.H., Xu, Z.Q., He, B.Z., and Wang, R.R. (2012) Age and tectonic evolution of ductile shear zones in the eastern Tianshan-Beishan orogenic belt. Acta Petrologica Sinica, v. 28, p. 1875–1895 (in Chinese with English abstract).

Chen, G. (2008) The mineralization characteristics and prospecting indicator of Lingyun copper deposit, Xinjiang. Xinjiang Geology, v. 26, p. 356–362 (in Chinese with English abstract).

Chen, H.Y., Chen, Y.J., and Michael, J.B. (2012a) Evolution of ore-forming fluids in the Sawayaerdun gold deposit in the Southwestern Chinese Tianshan metallogenic belt, Northwest China. Journal of Asian Earth Sciences, v. 49, p. 131–144.

Chen, H.Y., Chen, Y.J., and Michael, J.B. (2012b) Isotopic geochemistry of the Sawayaerdun orogenic-type gold deposit, Tianshan, northwest China: Implications for ore genesis and mineral exploration. Chemical Geology, v. 310–311, p. 1–11.

Chen, Y.J. (2006) Orogenic-type deposits and their metallogenic model and exploration potential. Geology in China, v. 33, p. 1181–1196 (in Chinese with English abstract).

Chen, Y.J., Pirajno, F., and Sui, Y.H. (2004) Isotope geochemistry of the Tieluping silver deposit, Henan, China: a case study of orogenic silver deposits and related tectonic setting. Mineralium Deposita, v. 39, p. 560–575.

Clayton, R.N., Mayeda, T.K. (1963) The use of bromine pentafluoride in the extraction of oxygen from oxides and silicates for isotopic analysis. Geochimica et Cosmochimica Acta, v. 27, p. 43–52.

Clayton, R. N., O'Neil, J. R., and Mayeda, T. K. (1972). Oxygen isotope exchange between quartz and water. Journal of Geophysical research, v. 77, p. 3057–3067.

Cline, J. S., and Bodnar, R. J. (1991) Can economic porphyry copper mineralization be generated by a typical calc-alkaline melt? Journal of Geophysical Research: Solid Earth, v. 96, p. 8113–8126.

Coleman, M.L., Sheppard, T.J., Durham, J.J., Rouse, J.E., and Moore, G.R. (1982) Reduction of water with zinc for hydrogen isotope analysis. Analytical Chemistry, 54, 993–995.

Drummond, S. E., and Ohmoto, H. (1985) Chemical evolution and mineral deposition in

boiling hydrothermal systems. Economic Geology, v. 80, p. 126–147.

Ding, Y., Veblen, D. R., and Prewitt, C. T. (2005) Possible Fe/Cu ordering schemes in the 2□ superstructure of bornite (Cu_5FeS_4). American Mineralogist, v. 90 (8–9): p. 1265–1269.

Etschmann, B. E., Liu, W., Testemale, D., Mueller, H., Rae, N. A., Proux, O., and Brugger, J. (2010) An in situ XAS study of copper (I) transport as hydrosulfide complexes in hydrothermal solutions (25–592 °C, 180–600 bar): speciation and solubility in vapor and liquid phases. Geochimica et Cosmochimica Acta, v. 74, p. 4723–4739.

Estrade, N., Carignan, J., Sonke, J.E., and Donard, O.F.X. (2009) Mercury isotope fractionation during liquid–vapour evaporation experiments. Geochimica et Cosmochimica Acta, v. 73, p. 2693–2711.

Gregory, M. J., and Mathur, R. (2017) Understanding copper isotope behavior in the high temperature magmatic-hydrothermal porphyry environment. Geochemistry, Geophysics, Geosystems, v. 18, p. 4000–4015.

Gao, J., Long, L.L., Klemd, R., Qian, Q., Liu, D.Y., Xiong, X.M., Su, W., Liu, W., Wang, Y.T., and Yang, F.Q. (2009) Tectonic evolution of the South Tianshan orogen and adjacent regions, NW China: geochemical and age constraints of granitoid rocks. International Journal of Earth Sciences, v. 98, 1221–1238.

Goh, S.W., Buckley, A.N., Lamb, R.N., Rosenberg, R.A. and Moran, D. (2006) The oxidation states of copper and iron in mineral sulfides, and the oxides formed on initial exposure of chalcopyrite and bornite to air. Geochimica et Cosmochimica Acta, v. 70, p. 2210–2228.

Golding, S.D., Groves, D.I., McNaughton, N.J., Mikucki, E.J. and Sang, J.H. (1990) Sulfur

isotope studies, in Ho, S.E., Groves, D.I. Bennett, J.M., eds., Gold deposits of the Archean Yilgarn Block, Western Australia: Nature, Genesis and Exploration Guides. University of Western Australia, Geology Department and University Extension Publication v. 20, p. 259–262.

Goldfarb, R. J., Ayuso, R., Miller, M. L., Ebert, S. W., Marsh, E. E., Petsel, S. A., and McClelland, W. (2004) The late Cretaceous Donlin Creek gold deposit, Southwestern Alaska: Controls on epizonal ore formation. Economic geology, v. 99, p. 643–671.

Goldfarb, R., Baker, T., Dube, B., Groves, D. I., Hart, C. J., and Gosselin, P. (2005) Distribution, character and genesis of gold deposits in metamorphic terranes. Economic Geology, 100th Anniversary Volume, p. 407–450.

Guo, H., Xia, Y., Bai, R., Zhang, X., and Huang, F. (2020). Experiments on Cu isotope fractionation between chlorine bearing fluid and silicate magma: implications for fluid exsolution and porphyry Cu deposits. National Science Review https://doi.org/10.1093/nsr/nwz221

Gruen, G., Weis, P., Driesner, T., Heinrich, C. A., & de Ronde, C. E. (2014). Hydrodynamic modeling of magmatic–hydrothermal activity at submarine arc volcanoes, with implications for ore formation. Earth and Planetary Science Letters, 404, p. 307–318.

Heinrich, C. A. (2005). The physical and chemical evolution of low-salinity magmatic fluids at the porphyry to epithermal transition: a thermodynamic study. Mineralium Deposita, v. 39(8), p. 864–889.

Heinrich C.A. (2007) Fluid-fluid interactions in magmatic- hydrothermal ore formation. In Fluid-Fluid Interactions. Reviews in Mineralogy and Geochemistry (eds. A. Liebscher

and C. A. Heinrich), pp. 363–387.

Heinrich, C.A., Ryan, C.G., Mernagh, T.P., Eadington, P.J. (1992). Segregation of ore metals between magmatic brine and vapor; a fluid inclusion study using PIXE microanalysis. Economic Geology, v. 87(6), p. 1566−1583.

Heinrich, C.A., Günther, D., Audétat, A., Ulrich, T., and Frischknecht (1999) Metal fractionation between magmatic brine and vapor determined by microanalysis of fluid inclusions. Geology, v. 26, p. 755−758.

Hoefs, J. (2009) Stable isotope geochemistry (vol. 285). Berlin. springer.

Hoefs, J. (2018) Stable isotope geochemistry (eighth edition). Berlin. springer.

Horita, J., and Wesolowski, D.J. (1994) Liquid-vapor fractionation of oxygen and hydrogen isotopes of water from the freezing to the critical temperature. Geochimica et Cosmochimica Acta, v. 58, p. 3425–3437.

Höhn, S., Frimmel, H. E., Debaille, V., Pašava, J., Kuulmann, L. and Debouge, W. (2017). The case for metamorphic base metal mineralization: pyrite chemical, Cu and S isotope data from the Cu-Zn deposit at Kupferberg in Bavaria, Germany. Mineralium Deposita, v. 52, p. 1145–1156.

Jiang, T., Gao, J., Klemd, R., Qian, Q., Zhang, X., Xiong, X., Wang, X.S., Tan, Z., and Chen, B. (2014) Paleozoic ophiolitic mélanges from the South Tianshan Orogen, NW China: Geological, geochemical and geochronological implications for the geodynamic setting. Tectonophysics, v. 612–613, p. 106–127.

Johnson, J.W., Oelkers, E.H., and Helgeson, H.C. (1992) Supcrt92–a Software package for calculating the standard molal thermodynamic properties of minerals, gases, aqueous

species, and reactions from 1-Bar to 5000-Bar and 0-degrees-C to 1000-degrees-C. Computer Geosciences, v. 18, p. 899–947.

Keppler, H., and Wyllie, P.J. (1991) Partitioning of Cu, Sn, Mo, W, U, and Th between melt and aqueous fluid in the systems haplogranite-H_2O-HCl and haplogranite-H_2O-HF. Contributions to Mineralogy and Petrology, v. 109, p. 139–150.

Kitt, S., Kisters, A., Steven, N., Maiden, K., and Hartmann, K. (2016) Shear-zone hosted copper mineralisation of the Omitiomire deposit–structural controls of fluid flow and mineralisation during subduction accretion in the Pan-African Damara Belt of Namibia. Ore Geology Reviews, v. 75, p. 1–15.

Konopelko, D., Biske, G., Seltmann, R., Eklund, O., and Belyatsky, B. (2007) Post-collisional granites of the Kokshaal Range, southern Tien Shan, Kyrgystan: petrogenesis and regional tectonic implications. Lithos, v. 4, p. 140–160.

Konopelko, D., Seltmann, R., Biske, G., Lepekhina, E., and Sergeev, S. (2009) Possible source dichotomy of contemporaneous post-collisional barren I-type versus tin-bearing A-type granites, lying on opposite sides of the South Tien Shan suture. Ore Geology Reviews, v. 35, p. 206–216.

Landtwing, M.R., Furrer, C., Redmond, P.B., Pettke, T., Guillong, M., and Heinrich, C.A. (2010) The Bingham Canyon porphyry Cu-Mo-Au deposit. III. Zoned copper-gold ore deposition by magmatic vapor expansion. Economic Geology, v. 105, p. 91–118.

Lerchbaumer, L., and Audétat, A. (2012). High Cu concentrations in vapor-type fluid inclusions: An artifact? Geochimica et Cosmochimica Acta, v. 88, p. 255–274.

Li, Y., and Audétat, A. (2012) Partitioning of V, Mn, Co, Ni, Cu, Zn, As, Mo, Ag, Sn, Sb, W,

Au, Pb, and Bi between sulfide phases and hydrous basanite melt at upper mantle conditions. Earth and Planetary Science Letters, v. 355, p. 327–340.

Li, Y., and Audétat, A. (2015) Effects of temperature, silicate melt composition, and oxygen fugacity on the partitioning of V, Mn, Co, Ni, Cu, Zn, As, Mo, Ag, Sn, Sb, W, Au, Pb, and Bi between sulfide phases and silicate melt. Geochimica et Cosmochimica Acta, v. 162, p. 25–45.

Li, W., Jackson, S.E., Pearson, N.J., and Graham, S. (2010) Copper isotopic zonation in the Northparkes porphyry Cu–Au deposit, SE Australia. Geochimica et Cosmochimica Acta v. 74, p. 4078–4096.

Liu, S.-A., Li, D.D., Li, S.G., Teng, F.Z., Ke, S., He, Y.S. and Lu, Y.H. (2014a) High-precision copper and iron isotope analysis of igneous rock standards by MC–ICP–MS. Journal of Analytical Atomic Spectrometry, v. 29, p. 122–133.

Liu, S.-A., Teng, F.Z., Li, S.G., Wei, G.J., Ma, J.L. and Li, D.D. (2014b) Copper and iron isotope fractionation during weathering and pedogenesis: Insights from saprolite profiles. Geochimica et Cosmochimica Acta, v. 146, p. 59–75.

Liu, S.-A., Huang, J., Liu, J.G., G. Wörner., Yang, W., Tang, Y.J., Chen, Y., Tang, L.-M., Zheng, J., and Li, S.-G. (2015) Copper isotopic composition of the silicate Earth. Earth and Planetary Science Letters, v. 427, p. 95–103.

Long, L.L., Gao, J., Klemd, R., Beier, C., Qian, Q., Zhang, X., Wang, J.B., and Jiang, T. (2011) Geochemical and geochronological studies of granitoid rocks from the Western Tianshan Orogen: Implications for continental growth in the southwestern Central Asian Orogenic Belt. Lithos, v. 126, p. 321–340.

McCuaig, T.C. and Kerrich, R. (1998) P-T-t-deformation-fluid characteristics of lode gold deposits: evidence from alteration systematics. Ore Geology Reviews, v. 12, 381–453.

Maréchal, C.N., Télouk, P., and Albarède, F. (1999) Precise analysis of copper and zinc isotopic compositions by plasma-source mass spectrometry. Chemical Geology, v. 156, p. 251–273.

Maher, K.C., and Larson, P.B. (2007) Variation in copper isotope ratios and controls on fractionation in hypogene skarn mineralization at Coroccohuayco and Tintaya, Peru. Economic Geology, v. 102, p. 225–237.

Maher, K. C., Jackson, S., and Mountain, B. (2011) Experimental evaluation of the fluid-mineral fractionation of Cu isotopes at 250°C and 300°C. Chemical Geology, v. 286, p. 229–239.

Mathur, R., Ruiz, J., Casselman, M. J., Megaw, P., and van Egmond, R. (2012) Use of Cu isotopes to distinguish primary and secondary Cu mineralization in the Canariaco Norte porphyry copper deposit, Northern Peru. Mineralium Deposita, v. 47, p. 755–762.

Mathur, R., Titley, S., Barra, F., Brantley, S., Wilson, M., Phillips, A., Munizaga, F., Maksaev, Vervoort, J., and Hart, G. (2009) Exploration potential of Cu isotope fractionation in porphyry copper deposits. Journal of Geochemical Exploration, v. 102, p. 1–6.

Mathur, R., Dendas, M., Titley, S., Philips, A. (2010) Patterns in the copper isotope composition of minerals in porphyry copper deposits in southwestern United States. Economic Geology, v. 105, p. 1457–1467.

Mathur, R., Munk, L., Nguyen, M., Gregory, M., Annell, H., and Lang, J. (2013) Modern and paleofluid pathways revealed by Cu isotope compositions in surface waters and ores of

the Pebble porphyry Cu-Au-Mo deposit, Alaska. Economic Geology, v. 108, p. 529–541.

Molnár, F., Mänttäri, I., O'Brien, H., Lahaye, Y., Pakkanen, L., Johanson, B., Käpyaho, Asko., Sorjonen-Ward, P., Whitehouse, M. and Sakellaris, G. (2016). Boron, sulphur and copper isotope systematics in the orogenic gold deposits of the Archaean Hattu schist belt, eastern Finland. Ore Geology Reviews, v. 77, p. 133–162.

Morelli, R., Creaser, R.A., Seltmann, R., Stuart, F., Selby, D., and Graupner, T., (2007) Age and source constraints for the giant Muruntau gold deposit, Uzbekistan, from coupled Re-Os-He isotopes in arsenopyrite. Geology, v. 35, p. 795–798.

Migdisov, A.A., Bychkov, A.Y., Williams-Jones, A.E., Van Hinsberg, V.J. (2014). A predictive model for the transport of copper by HCl-bearing water vapour in ore-forming magmatic-hydrothermal systems: Implications for copper porphyry ore formation. Geochimica et Cosmochimica Acta, v. 129, p. 33–53.

Ohmoto, H. (1986) Stable isotope geochemistry of ore deposits. Review in Mineralogy, 16, p. 491–559

Palin, J. M., and Xu, Y. (2000) Gilt by association? Origins of pyritic gold ores in the Victory mesothermal gold deposit, Western Australia. Economic Geology, v. 95, 1627–1634.

Pearce, C.I., Pattrick, R.A.D., Vaughan, D.J., Henderson, C.M.B., and van der Laan, G. (2006) Copper oxidation state in chalcopyrite: mixed Cu d^9 and d^{10} characteristics. Geochimica et Cosmochimica Acta, v. 70, p. 4635–4642.

Phillips, G.N., and Powell, R. (2009) Formation of gold deposits: Review and evaluation of the continuum model. Earth-Science Reviews, v. 94, p. 1–21.

Phillips, G. N., and Powell, R. (2010) Formation of gold deposits: a metamorphic

devolatilization model. Journal of Metamorphic Geology, v. 28, p. 689–718.

Pirajno, F. (2009) Hydrothermal Processes and Mineral System. Springer, Perth, p. 1–1250

Pirajno, F. (2010) Intracontinental strike-slip faults, associated magmatism, mineral systems and mantle dynamics: examples from NW China and Altay-Sayan (Siberia). Journal of Geodynamics, v. 50, p. 325–346.

Pirajno, F., Seltmann, R., and Yang, L.Q. (2011) A review of mineral systems and associated tectonic settings of northern Xinjiang, NW China. Geoscience Frontiers, v. 2, p. 157–185.

Pokrovski, G.S., Borisova, A.Y., and Harrichoury, J. (2008) The effect of sulfur on vapor-liquid fractionation of metals in hydrothermal systems. Earth and Planetary Science Letters, v. 266, p. 345–362.

Précigout, J., Prigent, C., Palasse, L., and Pochon, A. (2017) Water pumping in mantle shear zones. Nature Communications, v. 8, p. 1–10.

Qian, Q., Gao, J., Klemd, R., He. G.Q., Song, B., Liu, D.Y., and Xu, R.H. (2009) Early Paleozoic tectonic evolution of the Chinese South Tianshan Orogen: constraints from SHRIMP zircon U–Pb geochronology and geochemistry of basaltic and dioritic rocks from Xiate, NW China. International Journal of Earth Sciences, v. 98, p. 551–569.

Richet, P., Bottinga, Y., and Javoy, M. (1977) A review of hydrogen, carbon, nitrogen, oxygen, sulphur, and chlorine stable isotope fractionation among gaseous molecules. Annual Review of Earth and Planetary Sciences, v. 5, p. 65–110.

Rye, R.O. (1993) The evolution of magmatic fluids in the epithermal environment: The stable isotope perspective. Economic Geology, v. 88, p. 733–753.

Ohmoto, Hiroshi, R. O. Rye, and H. L. Barnes. (1979). Geochemistry of hydrothermal ore deposits. p. 509–567.

Sheppard, S.M.F., and Gustafson, L.B. (1976) Oxygen and hydrogen isotopes in the porphyry copper deposit at El Salvador, Chile. Economic Geology, v. 71, p. 1549–1559.

Rempel, K. U., Liebscher, A., Meixner, A., Romer, R. L., and Heinrich, W. (2012) An experimental study of the elemental and isotopic fractionation of copper between aqueous vapour and liquid to 450°C and 400 bar in the CuCl-NaCl-H_2O and CuCl-NaHS-NaCl-H_2O systems. Geochimica et Cosmochimica Acta, v. 94, p. 199–216.

Richter, F.M., Janney, P.E., Mendybaev, R.A., Davis, A.M., and Wadhwa, M. (2007) Elemental and isotopic fractionation of Type B CAI-like liquids by evaporation. Geochimica et Cosmochimica Acta, v. 71, p. 5544–5564.

Seo, J.H., and Heinrich, C.A. (2013). Selective copper diffusion into quartz-hosted vapor inclusions: Evidence from other host minerals, driving forces, and consequences for Cu–Au ore formation. Geochimica et Cosmochimica Acta, v. 113, p. 60–69.

Seo, J. H., Lee, S. K., and Lee, I. (2007) Quantum chemical calculations of equilibrium copper (I) isotope fractionations in ore-forming fluids. Chemical Geology, v. 243, p. 225–237.

Şengör, A.M.C., Natal'in, B.A., and Burtman, U.S. (1993) Evolution of the Altaid tectonic collage and Paleozoic crustal growth in Eurasia. Nature, v. 364, p. 209–304.

Sharp, Z. (2017) Principles of stable isotope geochemistry.

Shvarov, Y.V., and Bastrakov, E.N. (1999) HCh: A software package for geochemical equilibrium modelling. User's Guide. Australian Geological Survey Organization

Record 1999/25.

Sibson, R. H. (1986). Earthquakes and rock deformation in crustal fault zones. Annual Review of Earth and Planetary Sciences, v. 14, p. 149.

Sibson, R. H. (1987). Earthquake rupturing as a mineralizing agent in hydrothermal systems. Geology, v. 15, p. 701–704.

Sibson, R. H. (2004). Controls on maximum fluid overpressure defining conditions for mesozonal mineralisation. Journal of structural geology, v. 26, p. 1127–1136.

Sibson, R. H., Moore, J. M. M., Rankin, A. H. (1975). Seismic pumping-a hydrothermal fluid transport mechanism. Journal of the Geological Society, v. 131, p. 653–659.

Simon A. C., Pettke T., Candela P.A., Piccoli P.M. and Heinrich C.A. (2006) Copper partitioning in a melt–vapour–brine–magnetite–pyrrhotite assemblage. Geochimica et Cosmochimica Acta, v. 70, p. 5583–5600.

Sossi, P.A., Halverson, G.P., Nebel, O., and Eggins, S.M. (2015) Combined separation of Cu, Fe and Zn from rock matrices and improved analytical protocols for stable isotope determination. Geostandards Geoanalytical Research, v. 29, p. 12–149.

Taylor, H.P. (1974) The application of oxygen and hydrogen isotope studies to problems of hydrothermal alteration and ore deposition. Economic Geology, v. 69, p. 843–883.

Taylor, H.P. (1997) Oxygen and hydrogen isotope relationships in hydrothermal mineral deposits. In: Barnes HL (ed) Geochemistry of hydrothermal ore deposits, 3rd edn. Wiley, New York, p. 229–302.

Van der Laan, G., Pattrick, R.A.D., Charnock, J.M., and Grguric, B.A. (2002) $CuL_{2,3}$ x-ray absorption and the electronic structure of nonstoichiometric Cu_5FeS_4. Physical Review

B v. 66, p. 045104.

Wang, Z.C., Liu, J.M., Liu, H.T., Zeng, Q.D., Zhang, S., and Wang, Y.B. (2010) Complexity and uncertainty of tracing fluid sources by means of H-O, C, S, N isotope systems: a case study of orogenic lode gold deposits. Acta Petrologica et Mineralogica, 29, p. 563–576 (in Chinese with English abstract).

Wang, B., Shu, L.S., Cluzel, D., Faure, M., and Charvet, J. (2007) Geochemical constraints on Carboniferous volcanic rocks of the Yili Block (Xinjiang, NW China): Implication for the tectonic evolution of Western Tianshan. Journal of Asian Earth Sciences, v. 29, p. 148–159.

Wang, B., Faure, M., Shu, L.S., de Jong, K., Charvet, J., Cluzel, D., Jahn, B.M., Chen, Y., Ruffet, G. (2010) Structural and geochronological study of High-Pressure metamorphic rocks in the Kekesu section (Northwestern China): implications for the late Paleozoic tectonics of the southern Tainshan. Journal of Geology, v. 118, p. 59–77.

Wang, J., Davis, A.M., Clayton, R.N., Mayeda, T.K. and Hashimoto, A. (2001) Chemical and isotopic fractionation during the evaporation of the FeO–MgO–SiO_2–CaO–Al_2O_3–TiO_2 rare earth element melt system. Geochimica et Cosmochimica Acta, v. 65, p. 479–494.

Wang, Y.H., Xue, C.J., Liu, J.J., and Zhang, F.F. (2016a) Geological, geochronological, geochemical, and Sr-Nd-O-Hf isotopic constraints on origins of intrusions associated with the Baishan porphyry Mo deposit in eastern Tianshan, NW China. Mineralium Deposita, doi:10.1007/s00126-016-0646-z.

Wang, Y.H., Zhang, F.F., Liu, J.J., and Que, C.Y. (2016b) Carboniferous magmatism and mineralization in the area of the Fuxing Cu deposit, Eastern Tianshan, China: Evidence

from zircon U–Pb ages, petrogeochemistry, and Sr-Nd-Hf-O isotopic compositions. Gondwana Research, doi: 10.1016/j.gr.2016.03.007.

Wang, Y.H., Zhang, F.F., and Liu, J.J. (2016c) The genesis of the ores and intrusions at the Yuhai Cu-Mo deposit in eastern Tianshan, NW China: Constraints from geology, geochronology, geochemistry, and Hf isotope systematics. Ore Geology Reviews, v. 77: p. 312–331.

Wang, Y. H., Xue, C. J., Liu, J. J., and Zhang, F. F. (2018) Origin of the subduction-related Carboniferous intrusions associated with the Yandong porphyry Cu deposit in eastern Tianshan, NW China: constraints from geology, geochronology, geochemistry, and Sr–Nd–Pb–Hf–O isotopes. Mineralium Deposita, v. 53(5): p. 629–647.

Williams-Jones, A.E., and Heinrich, C.A. (2005) 100th Anniversary special paper: vapor transport of metals and the formation of magmatic-hydrothermal ore deposits. Economic Geology, v. 100, p. 1287–1312.

Williams-Jones, A.E., Migdisov, A.A. (2014) Experimental constraints on the transport and deposition of metals in ore-forming hydrothermal systems: Society of Economic Geologists, v. 18, p. 77–96.

Williams, H.M., and Archer, C. (2011) Copper stable isotopes as tracers of metal-sulphide segregation and fractional crystallisation processes on iron meteorite parent bodies. Geochimica et Cosmochimica Acta, v. 75, p. 3166–3178.

Windley, B.F., Alexeiev, D., Xiao, W.J., Kroner, A., and Badarch, G. (2007) Tectonic models for accretion of the Central Asian Orogenic Belt. Journal of the Geological Society, v. 164, p. 31–47.

Wilson, A., Cooke, D., Harper, B., and Deyell, C. (2007) Sulfur isotopic zonation in the Cadia district, southeastern Australia: exploration significance and implications for the genesis of alkalic porphyry gold–copper deposits. Mineralium Deposita, v. 42, p. 465–487.

Wombacher, F., Rehkamper, M., Mezger, K., Bischoff, A., and Mu¨nker, C. (2008) Cadmium stable isotope cosmochemistry. Geochimica et Cosmochimica Acta, v. 72, p. 646–667.

Xiao, W.J., Windley, B.F., Huang, B.C., Han, C.M., Yuan, C., Chen, H.L., Sun, M., Sun, S., and Li, J.L. (2009) End-Permian to mid-Triassic termination of the accretionary processes of the southern Altaids: implications for the geodynamic evolution, Phanerozoic continental growth, and metallogeny of Central Asia. International Journal of Earth Sciences, v. 98, p. 1189–1217.

Xu, Z.Q., Li, S.T., Zhang, J.X., Yang, J.S., He, B.Z., Li, H.B., Lin, C.S., and Cai, Z.H. (2011) Paleo-Asian and Tethyan tectonic systems with docking the Tarim block. Acta Petrologica Sinica, v. 27, p. 1–22 (in Chinese with English abstract).

Xue, C. J., Zhao, X. B., Zhao, W. C., Zhao, Y., Zhang, G.Z., Nurtaev, B., Pak, N., Mo, X.X. (2020). Deformed zone hosted gold deposits in the China-Kazakhstan-Kyrgyzstan-Uzbekistan Tian Shan: metallogenic environment, controlling parameters, and prospecting criteria. Earth Science Frontiers, v. 27, p. 294–319 (in Chinese with English abstract).

Yakubchuk, A., Cole, A., Seltmann, R., Shatov, V. (2002). Tectonic setting, characteristics, and regional exploration criteria for gold mineralization in the Altaid orogenic collage: the Tien Shan province as a key example. Society of Economic Geologists, v. 9, p.

177–202.

Yao, J., Mathur, R., Sun, W., Song, W., Chen, H., Mutti, L., and Luo, X. (2016) Fractionation of Cu and Mo isotopes caused by vapor-liquid partitioning, evidence from the Dahutang W-Cu-Mo ore field. Geochemistry, Geophysics, Geosystems, v. 17, p. 1725–1739.

Zajacz, Z., Candela, P. A., Piccoli, P. M. (2017). The partitioning of Cu, Au and Mo between liquid and vapor at magmatic temperatures and its implications for the genesis of magmatic-hydrothermal ore deposits. Geochimica et Cosmochimica Acta, v. 207, p. 81–101.

Zambardi, T., Sonke, J. E., Toutain, J. P., Sortino, F., and Shinohara, H. (2009) Mercury emissions and stable isotopic compositions at Vulcano Island (Italy). Earth and Planetary Science Letters, v. 277, p. 236–243.

Zhao, Y., Xue, C.J, Liu, S.-A., Symons, D.T., Zhao, X.B, Yang, Y.Q. and Ke, J.J. (2017) Copper isotope fractionation during sulfide-magma differentiation in the Tulaergen magmatic Ni–Cu deposit, NW China. Lithos, v. 286–287C, p. 206–215.

Zhao, Y., Xue, C. J., Huang, Y.S., Wang, X.F., Zhao, X.B., and Zhang, G.Z. (2018). A ductile to brittle shear zone–hosted Cu mineralization: Geological, geochronological, geochemical and fluid inclusion studies of the Lingyun Cu deposit, southern Tianshan, NW China. Ore Geology Reviews, v. 94, p. 155–171.

Zhao, Y., Xue, C. J., Liu, S. A., Mathur, R., Zhao, X. B., Yang, Y. Q., Dai, J.F., Man, R.H., and Liu, X.M. (2019) Redox reactions control Cu and Fe isotope fractionation in a magmatic Ni–Cu mineralization system. Geochimica et Cosmochimica Acta, v. 249, p. 42–58.

Zheng, Y. F. (1993) Calculation of oxygen isotope fractionation in hydroxyl-bearing silicates. Earth and Planetary Science Letters, v. 120, p. 247–263.

Zheng, Y., Zhang, L., Chen, Y.J., Qin, Y.J., and Liu, C.F. (2012) Geology, fluid inclusion geochemistry, and $^{40}Ar/^{39}Ar$ geochronology of the Wulasigou Cu deposit, and their implications for ore genesis, Altay, Xinjiang, China. Ore geology reviews, v. 49, p. 128–140.

Zhou, J.X., Wang, J.S., Yang, D.Z., and Liu, J.H. (2013) H-O-S-Cu–Pb isotopic constraints on the origin of the Nage Cu–Pb deposit, southeast Guizhou province, SW China. Acta Geologica Sinica-English Edition, v. 87, p. 1334–1343.

Zhong, R., Brugger, J., Tomkins, A. G., Chen, Y., and Li, W. (2015). Fate of gold and base metals during metamorphic devolatilization of a pelite. Geochimica et Cosmochimica Acta, v. 171, p. 338–352.

Zhu, X.K., O'Nions, R.K., Guo, Y., Belshaw, N.S., and Rickard, D. (2000) Determination of natural Cu-isotope variation by plasma-source mass spectrometry: implications for use as geochemical tracers. Chemical Geology, v. 163, p. 139–149.

Zhu, X.K., Guo, Y., Williams, R.J.P., O'Nions, R.K., Matthews, A., Burgess, B.K., and Salvato, B. (2002) Mass fractionation processes of transition metal isotopes. Earth and Planetary Science Letters, v. 200, p. 47–62.

Zimmer, K., Zhang, Y., Lu, P., Chen, Y., Zhang, G., Dalkilic, M., and Zhu, C. (2016) SUPCRTBL: A revised and extended thermodynamic dataset and software package of SUPCRT92. Computers and Geosciences, v. 90, p. 97–111.

Figure Captions

FIGURE 1 A. Simplified tectonic map of the Central Asian Orogenic Belt (modified from Sengör et al., 1993). **B**. Geological map of the Chinese Tianshan with orogenic Au deposits indicated (modified from Gao et al., 2009; Jiang et al., 2014). **C**. Geological map of the Lingyun deposit with cross-section A–A′ (**D**) indicated. Modified from the First Geological Team of the Xinjiang Bureau of Geology and Mineral Resources (2008).

FIGURE 2 Photographs and photomicrographs showing ore-bearing veins and sulfide mineral textures. **A**. Early-stage sulfide–quartz veins parallel to the foliation. **B**. Late-stage chalcopyrite–bornite–ankerite vein cutting the early-stage foliation. **C**. Early-stage sulfide mineral assemblages and silicate minerals showing a similar orientation. D. Sulfide mineral assemblages showing elongated shapes, with secondary chalcocite occurring at the edges of bornite. **E**. Inclusions of pyrite within chalcopyrite. **F**. The coexistence of chalcopyrite and bornite, with minor chalcopyrite exsolving from bornite. Secondary chalcocite occurs at the margins of, and fractures within, bornite. Abbreviations: Qtz = quartz, Ank = ankerite, Ser = sericite, Chl = chlorite, Ccp = chalcopyrite, Bn = bornite, Py = pyrite, Sil = silicate minerals, Sulf = sulfide minerals.

FIGURE 3 (A–B) Profile from prospecting line 90 to 146 showing the thickness of the orebody (**A**) and Cu grade (**B**); sample locations are indicated. **(C–F)** The variation in δD (**C**), $\delta^{18}O$ (**D**), $\delta^{34}S$ (**E**), and $\delta^{65}Cu$ (**F**) values from prospecting line 90 to line 138. The H–O isotopic compositions for metamorphic water are from Taylor (1974). The main geological

processes (red and green arrows and text) and key factors contributing to multiple isotope fractionations (black text) are indicated.

FIGURE 4 (**A**) Calculated $\delta^{18}O_{fluid}$ versus δD_{fluid} for early-stage quartz in the Lingyun deposit. Data for primary magmatic water, metamorphic water, and meteoric water are from Taylor (1974). The data for meteoric water from Tianshan are represented by H–O isotopic compositions in mid-latitude areas (Hoefs, 2009, 2018). (**B**) H–O isotopic composition and water–rock isotope exchange evolutional curves of the Lingyun deposit. The $\delta^{i}_{rock}{}^{18}O$ and $\delta^{i}_{rock}D$ values were set at 16‰ and −60‰ for the wall rocks, similar to the H−O compositions of spilite (Hoefs, 2009, 2018). (**C**) Modeling for vapor−liquid-separation-derived H isotope fractionation at variable temperatures. (**D**) Modeling of O isotope fractionation during vapor−liquid separation at variable temperature. (E–F) The H–O isotopic compositions of cumulative and instantaneous liquids and vapor under based on Rayleigh equations. The H–O isotope fractionation factors at 250 °C were estimated by the equations of Horita and Wesolowski (1994) (Equation 7–8). It was assumed that the H–O isotope fractionation factor remained constant during vapor liquidation. A histogram of the H–O isotope ratios for early-stage quartzes is also provided along the vertical axis for comparison.

FIGURE 5 Physiochemical modeling of hydrothermal assemblages in the Lingyun Fe–Cu–S–O–H mineralization system at (**A**) 350 °C, 200 bars (activities: Na 0.156, K 0.045, and Cl 0.201), (**B**) 300 °C, 200 bars (activities: Na 0.135, K 0.040, and Cl 0.182), and (**C**) 250 °C, 200 bars (activities: Na 0.127, K 0.035, and Cl 0.162). All diagrams were calculated

with $\alpha S = 0.1$, $\alpha Ca = 0.0001$, and $\alpha Mg = 0.0004$. Activities of Na, K, and Cl were calculated using the HCh modeling software (Shvarov and Bastrakov, 1999).

FIGURE 6 The S isotopic compositions of cumulative and instantaneous sulfides and fluid under reduced and oxidized conditions based on Rayleigh equations. The S isotope fractionation factors at 250 °C were estimated by the equations of Ohmoto and Rye (1979). It was assumed that the S isotope fractionation factor remained constant during sulfide precipitation. A histogram of the $\delta^{34}S$ range for sulfides is also provided along the vertical axis for comparison.

FIGURE 7 Plot of $\delta^{65}Cu$ values for coexisting chalcopyrite and bornite pairs in early-stage sulfide mineral-bearing quartz veins.

FIGURE 8 (**A**) Rayleigh distillation model of vapor-liquid partitioning of Cu isotopes showing the evolution of the liquid with $\delta^{65}Cu_{vapor} = -3‰$ and $\alpha_{vapor-liquid} = 0.998$ (Yao et al., 2016). (**B**) The Cu isotopic compositions of cumulative and instantaneous chalcopyrite and fluids based on Rayleigh equations. It was assumed that the Cu isotope fractionation factor remained constant during vapor–liquid separation and chalcopyrite precipitation. A histogram of the $\delta^{65}Cu$ range for sulfides and wall rocks are also provided along the vertical axis for comparison. Abbreviations: Early = Early-stage sulfides, Late = Late-stage sulfides.

FIGURE 9 (**A**) Schematic diagram showing fluid-flow pathways and associated H–O–S–Cu

isotopic compositions of the Lingyun deposit. The location of the cross-section for **Fig. 9B** is indicated. (**B**) Physiochemical conditions of fluids during their migration (see text for details).

TABLE 1. Hydrogen isotope ratios of fluid inclusions hosted by quartz and oxygen isotope ratios of quartz grains from the early-stage sulfide mineral-quartz veins in the Lingyun deposit, Eastern Tianshan, China.

Sample no.	Prospecting line no.	Fluid type	Vapor/liquid ratios	δD (‰)	$\delta^{18}O$ (‰)	Homogenization temperatures (°C)	Calculated $\delta^{18}O_{fluid}$ (‰)
L90-1	90	C, M	3:1−5:1	−100.5	10.8	240−279	1.6
L90-2	90	C, M	3:1−5:1	−102.4	10.9	248−275	1.8
L93-1	93	C, M, W	3:1−5:1	−100.5	11.9	240−275	2.8
L93-2	93	C, M	3:1−5:1	−95.6	10.5	249−279	1.4
L100-1	100	C, M	3:1−5:1	−100.8	11.1	245−260	2.3
L100-2	100	C, M, W	3:1−5:1	−103.9	10.6	245−265	1.5
L110-1	110	C, M	3:1−5:1	−82.5	10.5	255−275	1.9
L110-2	110	C, M	3:1−5:1	−92.4	10.3	251−276	1.7
L112-1	112	C, M	1:1−5:1	−80.3	10.8	255−270	2.4
L112-2	112	C, M	1:1−5:1	−90.7	10.3	250−270	1.8
L114-1	114	C, M	2:1−5:1	−88.3	12.2	250−268	3.7
L114-2	114	C, M, W	2:1−5:1	−96.5	8.9	255−270	0.5
L116-1	116	C, M	2:1−4:1	−78.3	13.2	258−270	4.9
L116-2	116	C, M	2:1−4:1	−88.5	10.5	245−288	1.9
L118-1	118	C, M, W	2:1−4:1	−84.3	13.4	245−289	4.9
L118-2	118	C, M, W	2:1−4:1	−87.6	11.1	248−268	2.5
L120-1	120	C, M, W	2:1−4:1	−85.2	12.9	245−275	4.2
L120-2	120	C, M, W	2:1−4:1	−86.8	12.1	255−278	3.6
L122-1	122	C, W	2:1−4:1	−80.3	13.9	250−275	5.3
L122-2	122	C, M, W	2:1−4:1	−79.5	12.2	255−295	3.7
L124-1	124	C, M, W	2:1−4:1	−82.9	13.7	245−275	5.2
L124-2	124	C, W	2:1−4:1	−84.5	13.2	254−277	4.5
L126-1	126	C, M, W	2:1−3:1	−74.7	14.9	255−290	6.3
L126-2	126	C, M, W	2:1−3:1	−81.8	14.3	265−285	6.2
L128-1	128	C, M, W	2:1−3:1	−75.4	13.4	265−295	5.7
L128-2	128	C, M, W	2:1−3:1	−77.2	14.4	275−300	7.0
L130-1	130	M, W	2:1−3:1	−71.7	14.9	280−320	8.0
L130-2	130	C, M, W	1:1−3:1	−68.9	13.5	305−329	7.2
L132-1	132	M, W	1:1−3:1	−70.2	12.9	309−337	6.9
L132-2	132	M, W	1:1−3:1	−68.9	13.2	310−335	7.0
L134-1	134	M, W	1:1−2:1	−60.5	13.9	326−339	8.1
L134-2	134	C, M, W	1:1−2:1	−63.5	14.5	306−335	8.5
L136-1	136	M, W	1:1−2:1	−62.2	14.9	305−345	9.3
L136-2	136	M, W	1:1−2:1	−63.1	15.6	316−349	9.9
L138-1	138	M, W	1:1−2:1	−61.5	14.5	320−357	8.8

L138-2	138	M, W	1:1−2:1	−61.2	14.0	310−365	8.7
L138-3	138	M, W	1:1−2:1	−60.1	14.8	305−369	9.7

Notes: The homogenization temperature of some fluid inclusions for calculating $\delta^{18}O_{fluid}$ is from Zhao et al. (2018). New data were analyzed following the same procedures. Secondary inclusions were carefully checked and avoided. The Lingyun deposit is composed of aqueous (liquid water and vapor water, W-type), mixed aqueous-carbonic (H_2O, CO_2 and minor N_2 phases, M-type) and pure carbonic (CO_2 with minor H_2O liquid and N_2 vapor, C-type) inclusions (Zhao et al., 2018).

920

TABLE 2. Copper and S isotopic compositions and Cu/Fe ratios of sulfide minerals and Cu and S isotopic compositions of wall rocks from the Lingyun deposit, Eastern Tianshan, China.

Sample no.	Sample types	Analyzed targets	Mineralization stage	Prospecting line no.	Elevation (m)	δ^{65}Cu (‰)	2SD	Cu/Fe ratios	δ^{34}S (‰)
L1-15	wall rock	whole-rock powder	−	124	1150	−0.63	0.06	n.d.	3.3
L1-11	wall rock	whole-rock powder	−	124	1150	−0.67	0.06	n.d.	5.0
L1-13	wall rock	whole-rock powder	−	128	1150	−0.64	0.06	n.d.	3.7
L1-18	wall rock	whole-rock powder	−	130	1150	−0.67	0.06	n.d.	6.6
L1-21	wall rock	whole-rock powder	−	100	1170	−0.65	0.06	n.d.	5.7
L1-23	wall rock	whole-rock powder	−	93	1170	−0.65	0.06	n.d.	6.1
L90-1	sulfide ores	chalcopyrite	Early	90	1190	−1.85	0.05	0.95	5.0
L90-2	sulfide ores	chalcopyrite	Early	90	1190	−1.65	0.05	0.96	2.0
L93-1	sulfide ores	chalcopyrite	Early	93	1190	−1.55	0.05	0.98	2.2
L93-2	sulfide ores	chalcopyrite	Early	93	1190	−1.62	0.05	0.96	3.7
L100-1	sulfide ores	chalcopyrite	Early	100	1190	−1.52	0.05	0.95	4.6
L100-2	sulfide ores	chalcopyrite	Early	100	1190	−1.45	0.05	0.97	2.9
L110-1	sulfide ores	chalcopyrite	Early	110	1170	−1.45	0.05	0.97	-3.3
L110-2	sulfide ores	chalcopyrite	Early	110	1170	−1.78	0.05	1.02	-7.2
L112-1	sulfide ores	chalcopyrite	Early	112	1150	−1.34	0.05	1.04	−4.2
L112-2	sulfide ores	chalcopyrite	Early	112	1150	−1.51	0.06	1.04	−8.0
L114-1	sulfide ores	chalcopyrite	Early	114	1150	−1.16	0.06	0.97	−1.8
L114-2	sulfide ores	chalcopyrite	Early	114	1150	−1.39	0.05	0.96	−5.5
L116-1	sulfide ores	chalcopyrite	Early	116	1150	−1.38	0.05	1.02	−5.2
L116-2	sulfide ores	chalcopyrite	Early	116	1150	−1.64	0.06	1.05	−1.2
L118-1	sulfide ores	chalcopyrite	Early	118	1150	−0.91	0.05	5.00	−6.1
L118-2	sulfide ores	chalcopyrite	Early	118	1150	−1.39	0.05	1.03	−8.1
L120-1	sulfide ores	chalcopyrite	Early	120	1150	−1.54	0.07	0.96	−4.3
L120-2	sulfide ores	chalcopyrite	Early	120	1150	−1.22	0.05	0.98	−7.2
L122-1	sulfide ores	chalcopyrite	Early	122	1150	−1.48	0.06	1.05	−4.6
L122-2	sulfide ores	chalcopyrite	Early	122	1150	−1.01	0.05	0.99	−8.1
L122-3	sulfide ores	chalcopyrite	Late	122	1150	0.05	0.05	0.93	−9.9
L124-1	sulfide ores	chalcopyrite	Early	124	1150	−1.15	0.06	0.92	−9.0
L124-2	sulfide ores	chalcopyrite	Early	124	1150	−0.95	0.05	0.98	−6.1

921

Table 2. Continued

Sample no.	Sample types	Analyzed targets	Mineralization stage	Prospecting line no.	Elevation (m)	δ^{65}Cu (‰)	2SD	Cu/Fe ratios	δ^{34}S (‰)
L124-3	sulfide ores	chalcopyrite	Early	124	1150	−1.22	0.05	0.96	−6.7
L126-1	sulfide ores	chalcopyrite	Early	126	1150	−1.12	0.05	0.95	−6.6
L126-2	sulfide ores	chalcopyrite	Early	126	1150	−1.05	0.05	0.97	−6.9
L126-3	sulfide ores	chalcopyrite	Late	126	1150	−0.05	0.05	0.97	−9.8
L128-1	sulfide ores	chalcopyrite	Early	128	1150	−1.02	0.05	0.97	−7.3
L128-2	sulfide ores	chalcopyrite	Early	128	1150	−0.88	0.05	1.02	−7.1
L128-3	sulfide ores	chalcopyrite	Late	128	1150	−0.15	0.06	0.99	−9.4
L130-1c	sulfide ores	chalcopyrite	Early	130	1150	−0.44	0.05	1.04	−7.8
L130-1b	sulfide ores	bornite	Early	130	1150	−0.27	0.06	5.04	−7.2
L130-2c	sulfide ores	chalcopyrite	Early	130	1150	−0.76	0.06	0.97	−8.8
L130-2b	sulfide ores	bornite	Early	130	1150	−0.39	0.05	4.96	−8.5
L132-1c	sulfide ores	chalcopyrite	Early	132	1150	−0.28	0.05	1.02	−6.6
L132-1b	sulfide ores	bornite	Early	132	1150	−0.33	0.06	5.05	−7.2
L132-2	sulfide ores	chalcopyrite	Late	132	1150	−0.15	0.05	0.98	−9.3
L134-1	sulfide ores	bornite	Early	134	1100	0.10	0.05	5.00	−9.1
L134-2c	sulfide ores	chalcopyrite	Early	134	1100	0.39	0.05	1.03	−8.7
L134-2b	sulfide ores	bornite	Early	134	1100	0.04	0.07	4.96	−9.3
L134-3	sulfide ores	chalcopyrite	Late	134	1100	−0.30	0.06	1.01	−11.2
L136-1c	sulfide ores	chalcopyrite	Early	136	1100	−0.32	0.05	0.98	−10.2
L136-1b	sulfide ores	bornite	Early	136	1100	−0.18	0.06	5.05	−10.6
L136-2c	sulfide ores	chalcopyrite	Early	136	1100	−0.01	0.05	0.99	−10.1
L136-2b	sulfide ores	bornite	Early	136	1100	0.05	0.05	4.93	−9.9
L138-1	sulfide ores	chalcopyrite	Early	138	1100	−0.28	0.05	1.03	−14.2
L138-2c	sulfide ores	chalcopyrite	Early	138	1100	−0.32	0.05	0.95	−14.1
L138-2b	sulfide ores	bornite	Early	138	1100	0.27	0.05	5.04	−14.3
L138-3	sulfide ores	bornite	Early	138	1100	−0.31	0.05	5.00	−14.1
L138-4	sulfide ores	chalcopyrite	Late	138	1100	−0.01	0.05	1.01	−10.8

Notes: The samples with the same number but different labels (e.g., L130-1c and L130-1b) represent the coexisting sulfide pairs. n.d. = not detected.

This is the peer-reviewed, final accepted version for American Mineralogist, published by the Mineralogical Society of America.
The published version is subject to change. Cite as Authors (Year) Title. American Mineralogist, in press.
DOI: https://doi.org/10.2138/am-2022-8888. http://www.minsocam.org/

Fig. 1

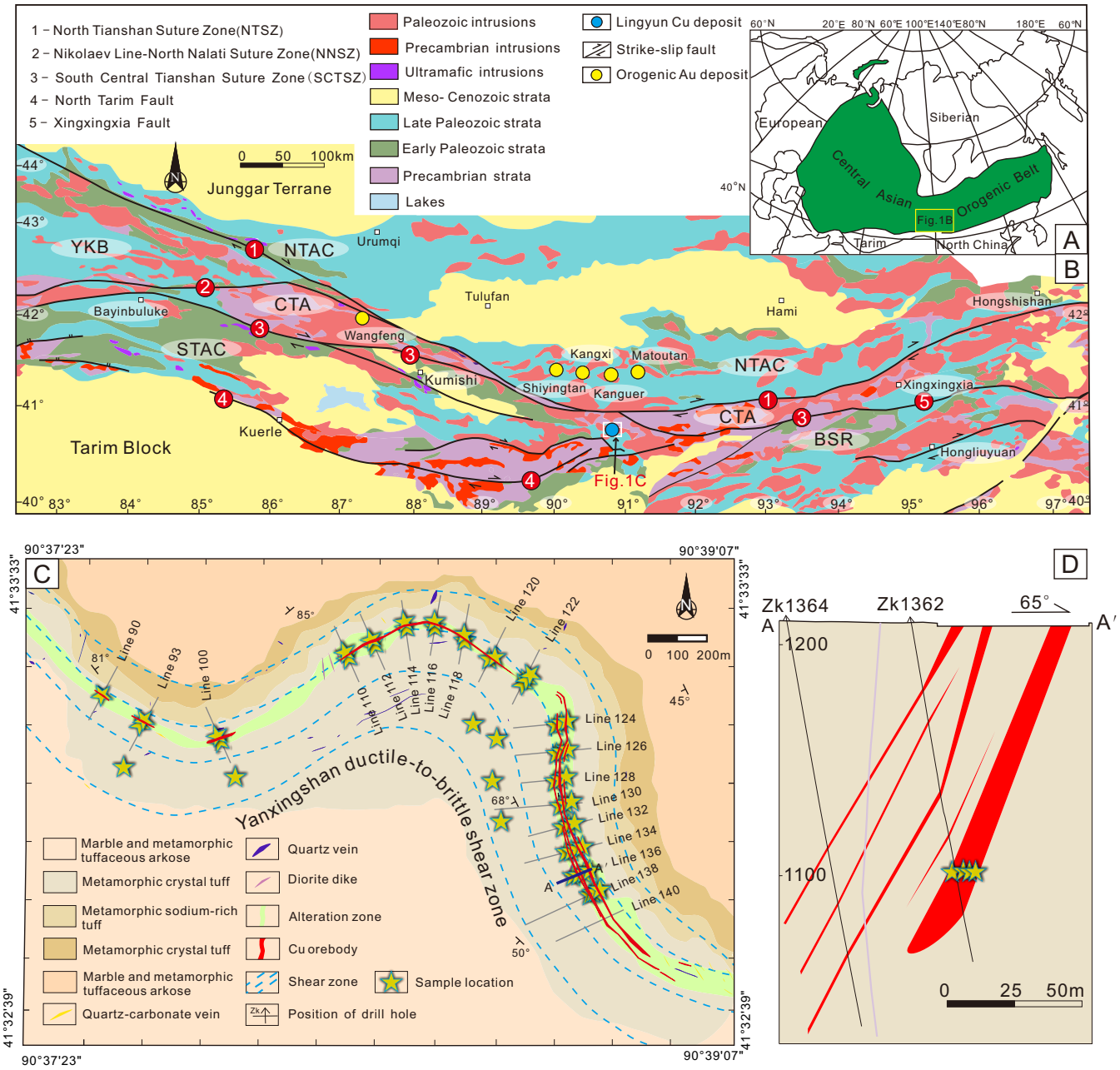

Fig. 2

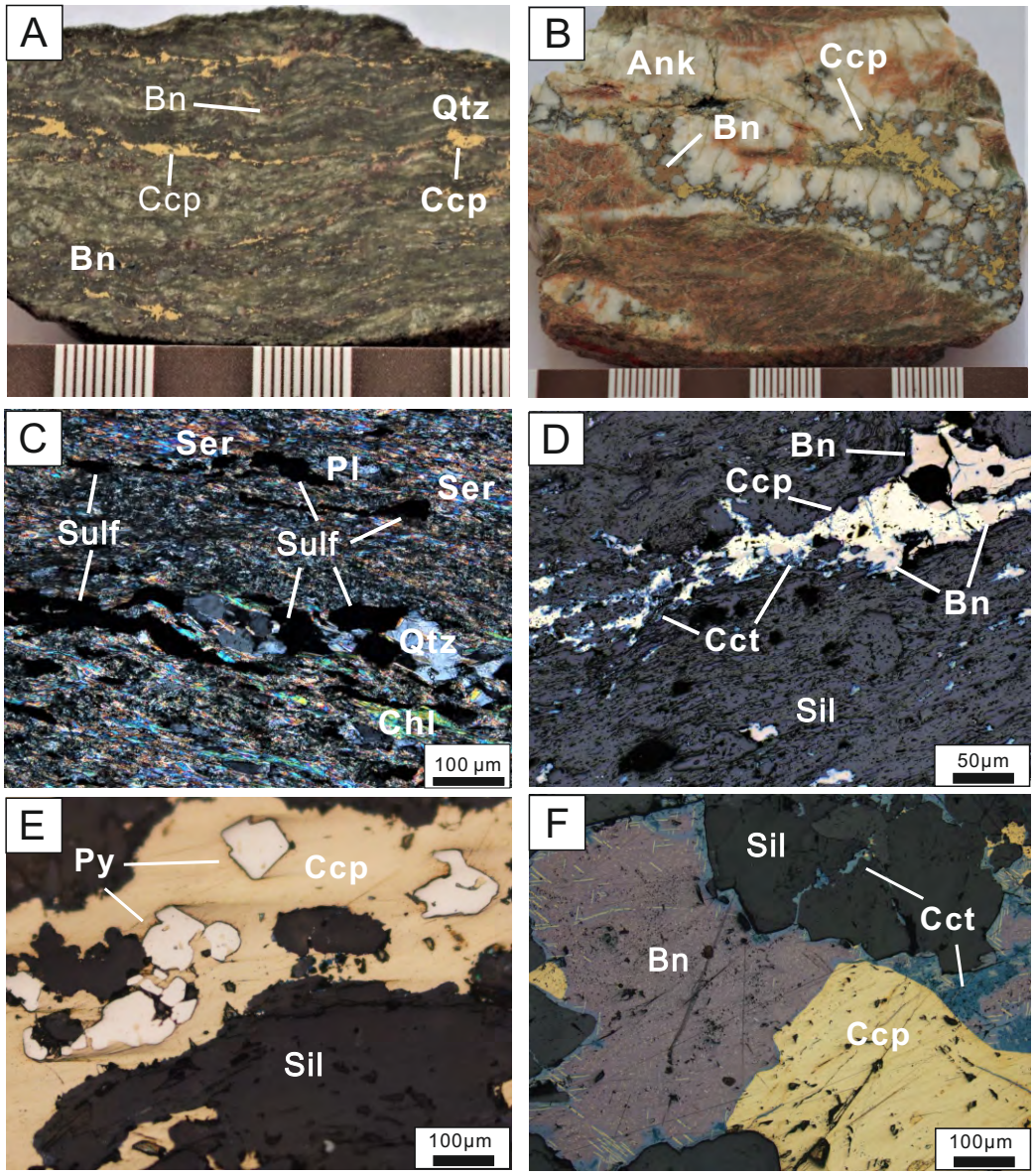

This is the peer-reviewed, final accepted version for American Mineralogist, published by the Mineralogical Society of America.
The published version is subject to change. Cite as Authors (Year) Title. American Mineralogist, in press.
DOI: https://doi.org/10.2138/am-2022-8888. http://www.minsocam.org/

Fig. 3

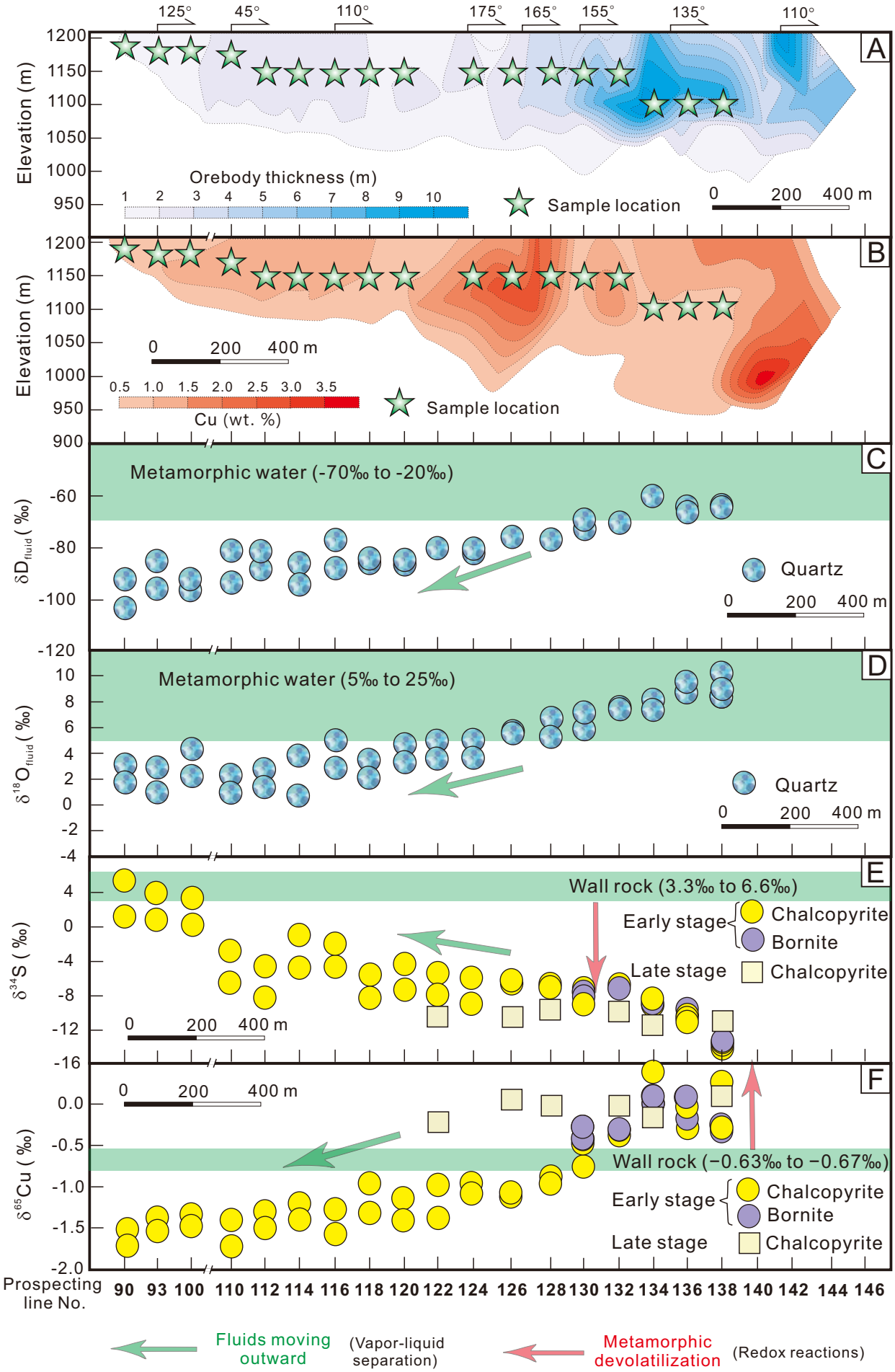

This is the peer-reviewed, final accepted version for American Mineralogist, published by the Mineralogical Society of America.
The published version is subject to change. Cite as Authors (Year) Title. American Mineralogist, in press.
DOI: https://doi.org/10.2138/am-2022-8888. http://www.minsocam.org/

Fig. 4

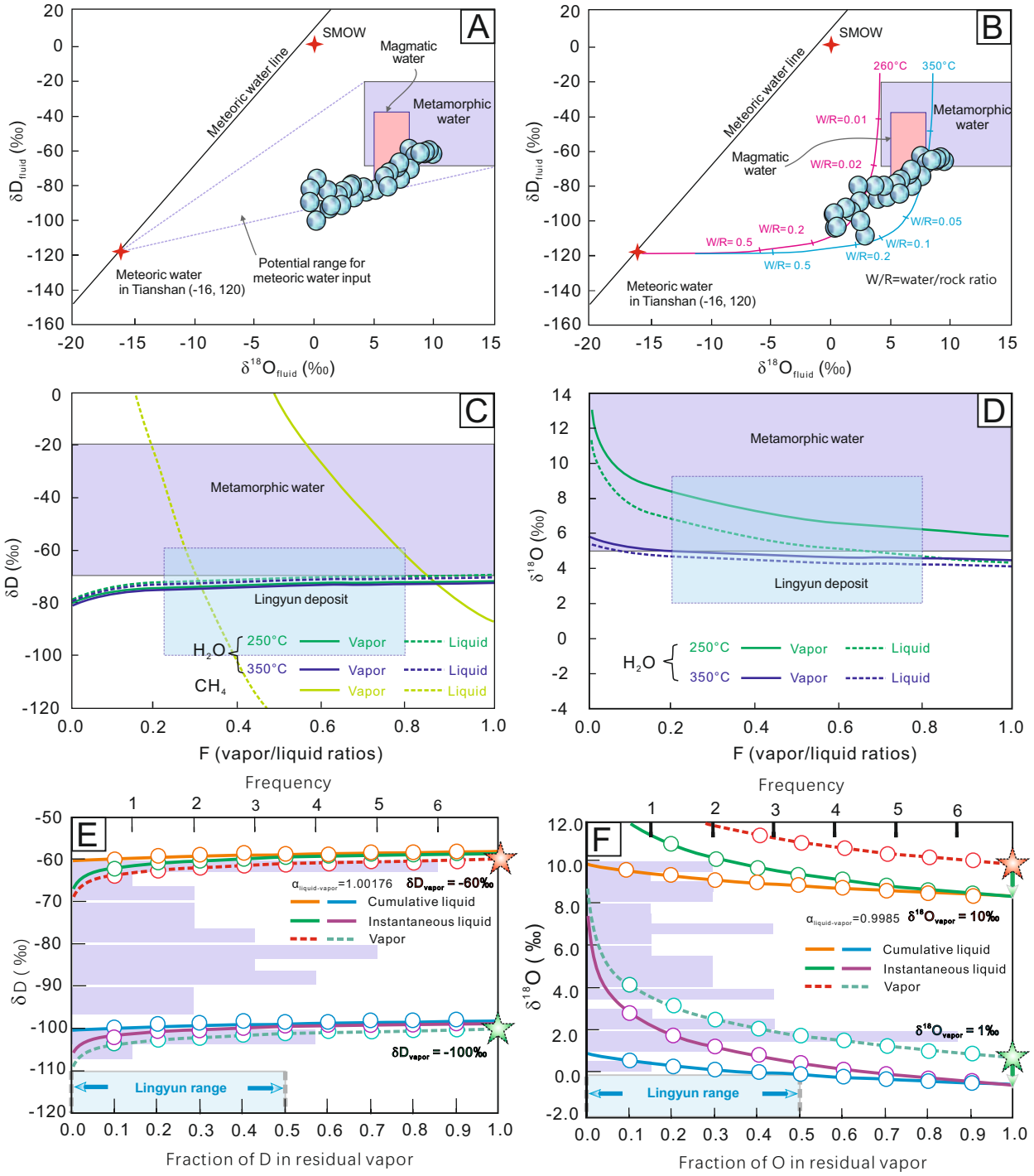

This is the peer-reviewed, final accepted version for American Mineralogist, published by the Mineralogical Society of America.
The published version is subject to change. Cite as Authors (Year) Title. American Mineralogist, in press.
DOI: https://doi.org/10.2138/am-2022-8888. http://www.minsocam.org/

Fig. 5

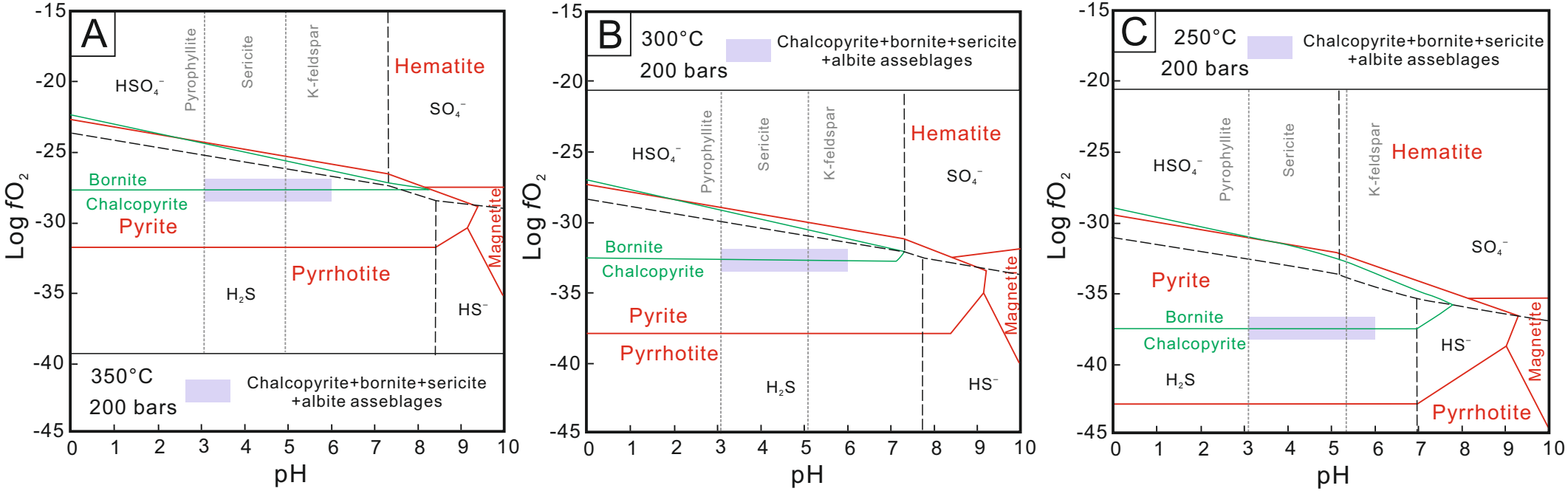

This is the peer-reviewed, final accepted version for American Mineralogist, published by the Mineralogical Society of America.
The published version is subject to change. Cite as Authors (Year) Title. American Mineralogist, in press.
DOI: https://doi.org/10.2138/am-2022-8888. http://www.minsocam.org/

Fig. 6

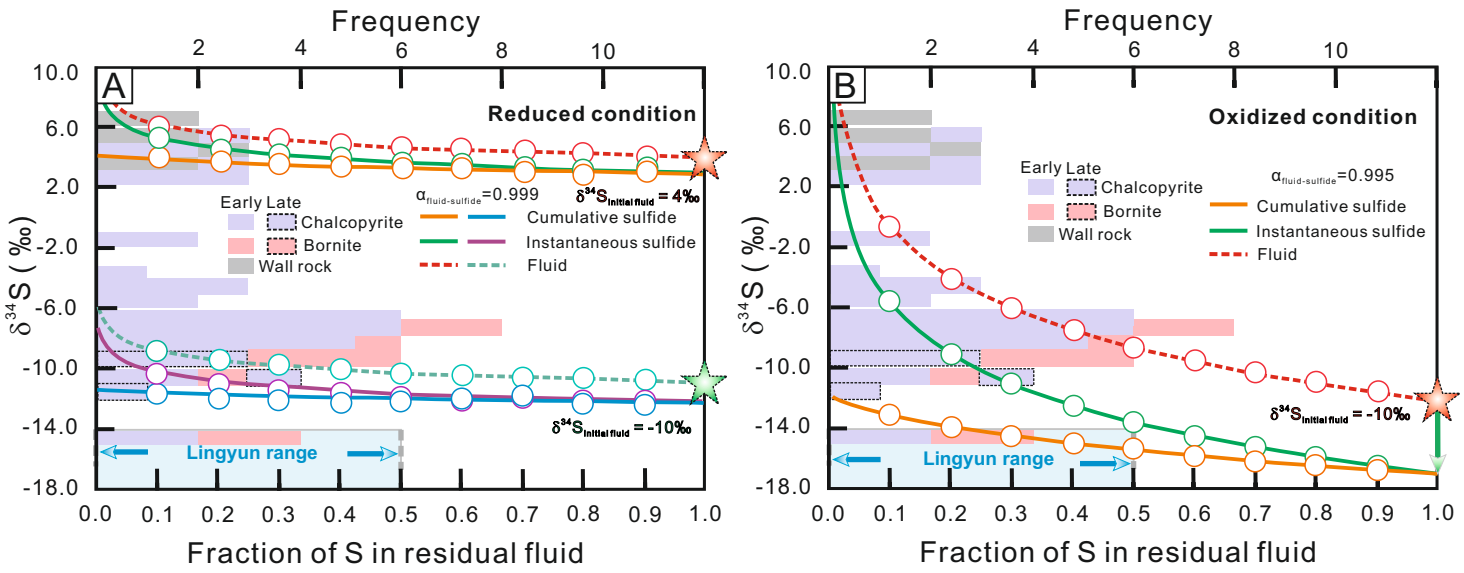

Fig. 7

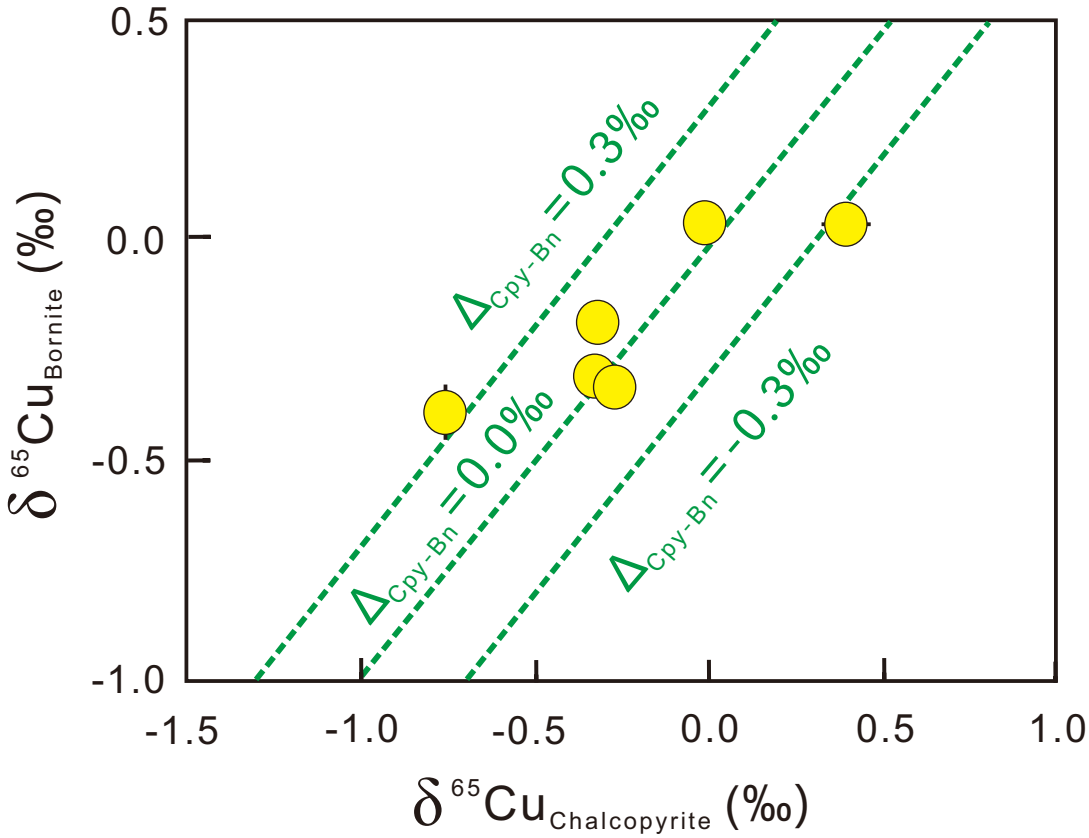

Fig. 8

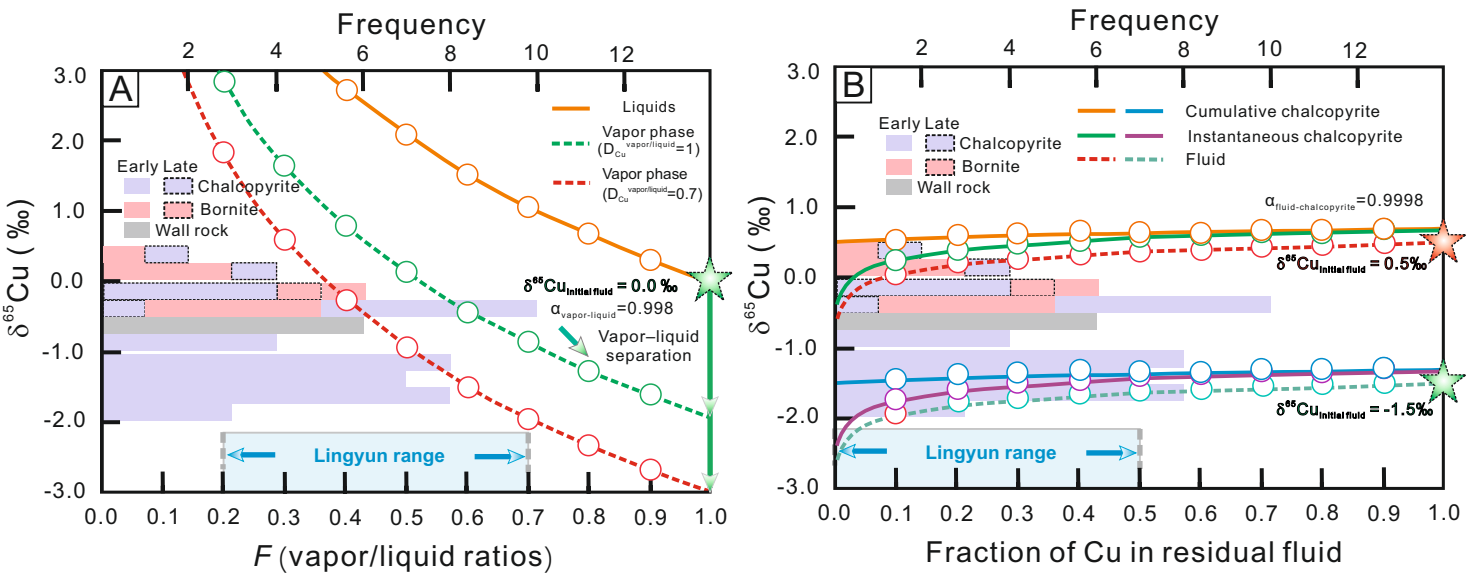

This is the peer-reviewed, final accepted version for American Mineralogist, published by the Mineralogical Society of America.
The published version is subject to change. Cite as Authors (Year) Title. American Mineralogist, in press.
DOI: https://doi.org/10.2138/am-2022-8888. http://www.minsocam.org/

Fig. 9